

**TOWARDS MRI-GUIDED AND ACTUATED  
TETHERLESS MILLI-ROBOTS: PREOPERATIVE  
PLANNING AND MODELING OF CONTROL**

---

A Thesis Presented to  
the Faculty of the Department of Computer Science  
University of Houston

---

In Partial Fulfillment  
of the Requirements for the Degree  
Master of Science

---

By  
Thibault Kensicher  
May 2017

**TOWARDS MRI-GUIDED AND ACTUATED  
TETHERLESS MILLI-ROBOTS: PREOPERATIVE  
PLANNING AND MODELING OF CONTROL**

---

Thibault Kensicher

APPROVED:

---

Nikolaos V. Tsekos  
Department of Computer science

---

Aaron T. Becker  
Department of Electrical Engineering

---

Ernst L. Leiss  
Department of Computer Science

---

Dean, College of Natural Sciences and Mathematics

### *Acknowledgements*

The work presented in this document was realized in collaboration with Prof Nikolaos V. Tsekos, of the Dept. of Computer Science and Dr. Aaron T. Becker and Dr. Julien Leclerc of the Dept. of Electrical Engineering in the University of Houston. Part of this document was submitted to the 2017 IEEE/RSJ International Conference on Intelligent Robots and Systems (IROS 2017).

My main contribution in this project was to the image processing and segmentation side, as well as the path planning process. All my thanks go to the member of the team for their invaluable help.

**TOWARDS MRI-GUIDED AND ACTUATED  
TETHERLESS MILLI-ROBOTS: PREOPERATIVE  
PLANNING AND MODELING OF CONTROL**

---

An Abstract of a Thesis

Presented to

the Faculty of the Department of Computer Science

University of Houston

---

In Partial Fulfillment

of the Requirements for the Degree

Master of Science

---

By

Thibault Kensicher

May 2017

# Abstract

Image-guided and robot-assisted surgical procedures are rapidly evolving due to their potential to improve patient management and cost effectiveness. Magnetic Resonance Imaging (MRI) is used for pre-operative planning and is also investigated for real-time intra-operative guidance. A new type of technology is emerging that uses the magnetic-field gradients of the MR scanner to maneuver ferromagnetic agents for local delivery of therapeutics. With this approach, MRI is both a sensor and forms a closed-loop controlled entity that behaves as a robot (we refer to them as MRbots). The objective of this thesis is to introduce a computational framework for preoperative planning using MRI and modeling of MRbot maneuvering inside tortuous blood vessels. This platform generates a virtual corridor that represents a safety zone inside the vessel that is then used to access the safety of the MRbot maneuvering. In addition, to improve safety we introduce a control that sets speed based on the local curvature of the vessel. The functionality of the framework was then tested on a realistic operational scenario of accessing a neurological lesion, a meningioma. This virtual case study demonstrated the functionality and potential of MRbots as well as revealed two primary challenges: real-time MRI (during propulsion) and the need of very-strong gradients for small MRbots for maneuvering inside narrow cerebral vessels. Our ongoing research focuses on further developing the computational core, MR tracking methods, and on-line interfacing to the MR scanner.

# Contents

<b>1</b>	<b>Introduction</b>	<b>1</b>
<b>2</b>	<b>Background</b>	<b>6</b>
2.1	MRI-driven devices . . . . .	7
2.2	Image segmentation . . . . .	8
<b>3</b>	<b>Methods</b>	<b>11</b>
3.1	Overview of the VF approach . . . . .	11
3.2	Computational framework . . . . .	12
3.3	Preoperative imaging processing module . . . . .	13
3.4	Planner module . . . . .	19
3.5	Control module . . . . .	26
3.6	Visualization module . . . . .	27
<b>4</b>	<b>Algorithms</b>	<b>28</b>
4.1	PIP module – Region-Growing algorithm . . . . .	28
4.2	PL module – Dijkstra’s algorithm . . . . .	29
4.3	Control module . . . . .	32
<b>5</b>	<b>Modelization, simulation, and results</b>	<b>33</b>
5.1	Modelization of the physical system . . . . .	33

5.2 Simulation Results . . . . .	34
<b>6 Conclusion</b>	<b>38</b>
<b>Bibliography</b>	<b>42</b>

# List of Figures

1.1	MR-based servoing of the MRbots (a) From the segmented vessel $OBJ(2, r)$ is extracted the Path $P(r)$ ; the virtual guidance corridor $GC(r)$ (dashed circle) is generated with a safety zone $S_Z$ . (b) The $GC(r)$ imposes a forbidden boundary beyond which the MRbot should not stray. (c) The gradient exerted force $F_G$ analyzed in two components, a propulsion $F_P$ and a correction transverse $F_T$ . . . . .	2
2.1	Contrasted MR imaging of a patient with a brain tumor: it appears in bright intensity on left side, while the edema results in a darker intensity, surrounding the tumor up and right on the image. . . . .	10
3.1	Architecture of the core (refer to Table 1 for definitions) of the system depicting processes and data flow paths among them. PIPm: Preoperative imaging processing module; PLm: Planner module; CNRm: control module; VISm: visualization module. . . . .	13
3.2	Representative input and output data of the PIPm showing a zoomed in area of the original DICOM image (95th slice of the TOF-MRA set that depicts three cerebral vessels (1)-(3)). The solid line is the output of the PIPm segmentation and the dashed circle is the maximum CG circle for vessel (1). Vessel (1) is the one that reaches the lesion and inside which the MRbot maneuvers. (b) Output of the PLm showing the segmented vessels and the CG mesh for vessel (1); this output is sent to the CNRm and VISm. No smoothing or interpolation was used, clearly demonstrating the challenge with native limited resolution of MR data. . . . .	16
3.3	Comparison between the manual results obtained without (in blue) and with the help of the Frangi filter (in cyan) . . . . .	18

3.4	Registered skin from both the TOF MRA scan in blue and the post-contrast T1w-FFE scan in green. . . . .	20
3.5	(a-b) 3D scene showing (a) 3D rendered vessels and meningioma and (b) the extracted path $P(r)$ from the inlet to the targeted sites. All 3D structures are inherently registered and scaled to the MR scanner coordinate system. No smoothing or interpolation was used. . . . .	21
3.6	Comparison of deformation due to imperfection between the shortest-path algorithm in blue, and the geometrical center-line in red. . . . .	23
3.7	Comparison between the original path in blue and the generated corrected path using the b-spline in red. . . . .	24
3.8	Image showing the different layers of the path planning. From bottom left to top right: Vascular tree, feeding artery, tube, safety corridor, path . . . . .	25
3.9	Diagram presenting the architecture of the trajectory controller. . . . .	27
5.1	Results of the simulation of the system. (a), (b) and (c) present the gradients generated by the MRI scanner for each axis. (d) is a plot of the curvature of the path. (e) shows the velocity of the MRbot and (f) compares the positioning error (red curve) with the maximum acceptable error (blue curve). The sphere is inside the guidance corridor when the red curve is below the blue curve. The MRbot stays in the corridor during the complete navigation. . . . .	35
5.2	3D plot of the trajectory of the sphere. The graph shows the planed trajectory $P(r)$ (blue line) and the actual trajectory (red line). . . . .	36

# List of Tables

3.1	Data used by the computational core. . . . .	14
-----	--	----

# Chapter 1

## Introduction

As minimally invasive procedures with real-time image guidance are emerging in the clinical realm, an ever-growing body of literature supports the potential of magnetic resonance targeting (MRT) to maneuver tiny tetherless therapeutic entities inside natural body pathways (such as vessels) to a targeted pathologic locus. MRT offer unparalleled potential to improve patient outcome. It is based on using the magnetic field gradients of an MRI scanner, used for signal spatial encoding and image generation, to propel and accurately maneuver a ferromagnetic object [17, 27, 69]. The fundamental benefit of MRT is its tetherless nature: no catheters, guidewires or other mechanical support that can harm tissue is needed; this is of paramount importance especially for paths inside small vessels (brain arteries) or quickly moving vessels (coronary arteries). The potential success of MRT can be transformative and eventually a paradigm shift for a plethora of interventions. This argument is eloquently stated by Sitti et al. [97]: “One of the highest potential scientific and

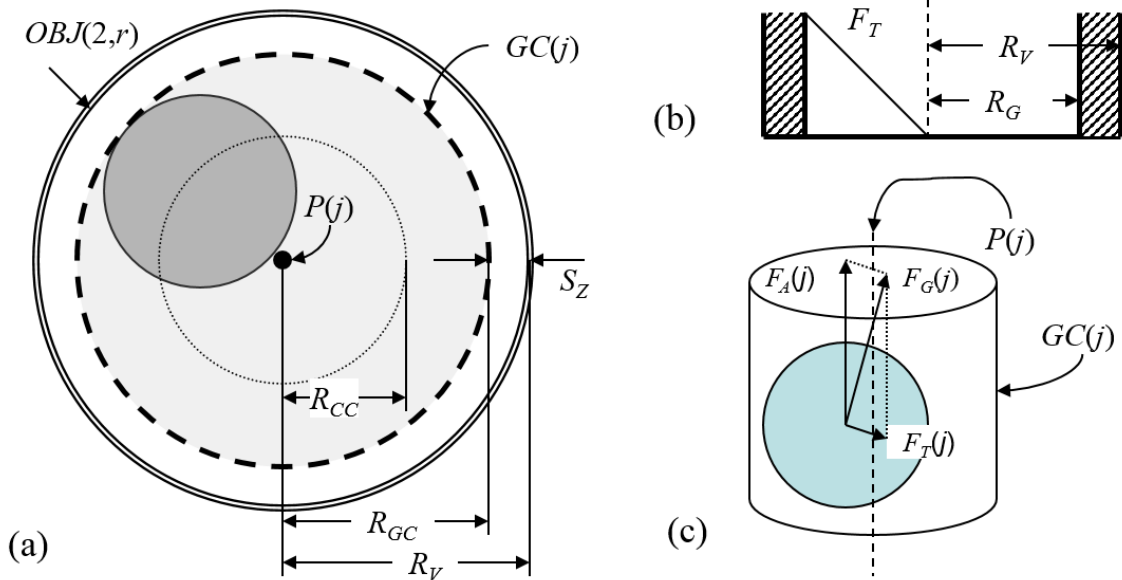


Figure 1.1: MR-based servoing of the MRbots (a) From the segmented vessel  $OBJ(2,r)$  is extracted the Path  $P(r)$ ; the virtual guidance corridor  $GC(r)$  (dashed circle) is generated with a safety zone  $S_Z$ . (b) The  $GC(r)$  imposes a forbidden boundary beyond which the MRbot should not stray. (c) The gradient exerted force  $F_G$  analyzed in two components, a propulsion  $F_P$  and a correction transverse  $F_T$ .

societal impacts of small-scale (millimeter and submillimeter size) untethered mobile robots would be their healthcare and bioengineering applications”. We have a system that operates in a closed loop using the MR scanner (i.e., its gradients and data acquisition) in this dual role to propel and track these entities. This system behaves and can be described as a robotic system. If we consider that we often have an assembly of such entities then we have a unique paradigm of robotic swarms driven by a single source [9]. For simplicity in this article we will refer to them as the MRbots. As it is well recognized by the pioneers in MRT [15, 40, 63, 75, 77, 106, 114] the most critical aspects are relating to the MRI modality: (i) as a sensor, the nuclear magnetic-resonance phenomenon is inherently of low-signal sensitivity, and (ii)

the imaging gradients are used for both propulsion and sensing. The result of the former is a practical trade-off between temporal and spatial resolution and both are essential for maneuvering inside vessels, especially in tortuous vessels, as well as in moving anatomies, such as the heart and the coronary arteries.

The above-mentioned clinical paradigms have the potential to highly benefit from this robotic technology. To ensure safety and accuracy, such procedures require continuous on-the-fly imaging (to both track the MRbots and image the pathway) and propulsion. For the purpose of MRbot control, this challenge can be appreciated considering that even a high resolution MRI, e.g., pixel sizes 0.25 to 0.5 mm, may not be sufficient to accurately image a 1-2 mm diameter vessel; this is highly demanding considering that in vivo the vessel is a 4D structure. In the absence of propulsion, practical real-time MRI (rt-MRI) can be achieved even with multislice MRI as was shown in cardiovascular procedures [2, 110]. The challenge is that with MRbots the gradients are also used for propulsion and there is a priority conflict: one needs to safely maneuver, which in turn requires continuous MRbot tracking and path imaging.

Prior groundbreaking in vivo and in vitro works have controlled the MRbots along a path between waypoints, for example [67]. Recently a study described a fast method to combine the propulsion and tracking [26]; still we are lacking intra-operative path imaging and the need to follow a trajectory without knowledge of consequences of an error. Alternative approaches need to be considered paving the way toward such in vivo interventions. A method complementary to trajectory planning, which requires accurately following a well predefined path to ensure safety, is to

control the MRbot to maneuver inside the tubular corridor defined by the vessel itself. Maneuvering inside a corridor that is narrower than the vessel offers a margin of error without colliding or perforating the vessel wall. This concept has been explored before in catheter-based vascular and cardiac interventions introducing virtual fixtures (VF), i.e., imaging-based software-generated virtual constraints, for improving safety and accuracy of telemanipulation systems [13, 15, 40, 75, 94, 106, 114]. Such an approach can address the limited spatial resolution of preoperative and intraoperative MRI as shown before in cardiac interventions [15, 40, 75]. From the large number of pioneering works in VF robot guidance, we review a small pertinent sample. Park et al. first introduced the innovative concept of VF for cardiac surgeries (coronary artery bypass graft procedures) using computed tomography (CT) images [106]. An important contribution was by Ren et al. that introduced the concept of dynamic virtual fixtures, generated by creating a visual/haptic model from preoperative dynamic MR/CT images and registering it using intraoperative ultrasound images, for minimally invasive robot assisted cardiac surgeries [114]. Yeniaras et al. described the generation of dynamic deformable volumes inside the left ventricle of the heart for safe access to the aortic root using pre-operative and single slice rt-MRI [15]. Navkar et al. introduced the use of multislice rt-MRI to update a 4D virtual corridor on-the-fly [40] and force-feedback interactive control [77] for intracardiac surgeries, that was then combined into an integrated framework for rt-MRI/VF-based robot control [63]. These, as well as other works in medicine or other control domains, demonstrated the value of virtual cues generated from imaging to guide a manual or robotic procedure.

This work is a first step toward building a system for performing tetherless MRbot interventions from the MRI servoing perspective. It focuses on implementing a prototype computational framework for MRI/VF-based visual-servoing of tetherless MRbots. It introduces the use of VF, extracted from pre-operative multi-contrast MRI, to generate virtual guidance cues for maneuvering MRbots inside tortuous vessels: 1) a guidance path along the centerline of the vessel which act as the preferred trajectory, and 2) a virtual guidance corridor that follows the guidance path with diameter adjusted to be smaller than the vessel diameter locally (within which the MRbot can safely maneuver, see Fig. 1.1). The guidance cues are then used by (1) the gradient generation module to calculate the needed magnetic force exerted onto the MRbot and generate the corresponding gradient waveforms and (2) the closed-loop speed and position controller. Those cues are in a format ready to provide visual cues to the operator via a display or augmented reality devices. Since on-line access to an MRI scanner was not available, this prototype framework was tested *in silico* simulating the maneuvering of a hollow sphere from an entrance location to a targeted lesion for the clinical paradigm of brain meningioma. Section 3 describes the implemented framework, Section 4 introduces the pseudo-code of the major methods used in this project, Section 5 describes and presents results from the *in silico* studies and Section 6 discusses the system and its limitations and concludes and discusses future works.

# Chapter 2

## Background

In this thesis we will explore a multi-disciplinary framework to plan and operate medical interventions using a Cyber-Physical System (CPS). Used as an alternative to conventional minimally-invasive operations and open-surgery, the frameworks operate in the field of computer and robot assisted interventions. A large number of methods were presented using robotic manipulators [4–6, 15, 16, 18, 28, 32, 38–40, 44, 45, 47, 54, 55, 61, 63, 68, 75, 77, 90, 106, 110, 111, 114], computational systems [2, 13, 94, 110] and haptic devices [11, 105, 110].

The system shown here and on which we will focus is used in the case of a brain tumor treatment through localized drug delivery, but could be extended to other applications including, but not limited to, remote biopsy, radiofrequency ablation, etc.

## 2.1 MRI-driven devices

Using the MRI scanner as both imaging machine and actuator would allow to perform surgery with a depth of visual feedback and precision not yet allowed with conventional open or minimally invasive surgery, or a safety unobtainable through X-ray guided surgery. The applications would range from minimally invasive surgery [10, 70, 117, 119] to drug and material delivery to specific and sensitive parts of the anatomy [14, 21, 30, 33, 34, 65, 66, 71, 104]. Driving tools using controlled magnetic fields introduced a new set of devices both for diagnostic and surgical procedures. Such tools were guided using different field generators coupled with various imaging techniques [107, 108, 119], from permanent magnet to control endoscope to survey localized destination [107, 118] to more complex electromagnetic actuators directing microrobots within vessels or fragile regions [19, 108, 119]. If these customized systems allow more freedom for development, they lack the duality the MRI has to offer to act both towards driving the tool and visualizing in near-real time the result. Moreover, an MRI machine allows fine tissue imaging without the danger of radiation inherent in X-rays systems. The electromagnetic fields of the MRI can be used to directly apply forces on ferromagnetic material through gradient manipulation [17, 27, 69], by inducing a current within embedded micro-coils allowing the robots to swim to their designated target [53, 67], or even steering catheter to its destination [57].

However, the nature of MRI raised several issues regarding image-guided operations [29, 41, 67, 112, 113]: Magnetic interactions between ferrous devices due their magnetization, heat generation through induced current in permissible metals, and imaging artifacts. Restricted by such complications, the cost of MR-compatible

robots was impacted and resulted in high-priced devices that need to be tethered to the external control systems [89, 99, 102].

## 2.2 Image segmentation

The scope of medical image segmentation, due to the numerous applications possible, results in a high number of proposed methods [79, 85, 87, 92]. Such techniques are improved every day to help physicians and surgeons reach faster decisions concerning diagnosis and prognostics. Whether built to quicken the detection of emerging disease on the anatomy scale [22–24, 48, 101, 115] or the cellular level [72, 84, 93], to guide the planning of a difficult operation [20, 62, 64, 109], or to follow a patient and prevent post-surgery complication [12, 50, 64], medical image processing can intervene in various stages of the curing process, allowing a substantial gain of time and information enhancing the patient healthcare.

Imaging of the brain to detect tumor is no exception to this rule [8, 35] and new and improved methods are introduced every week [3, 78, 82] to tackle this disease. If either mono- [76, 81] or multi-modality [46, 52, 83] imaging is crucial to diagnose brain tumor, MR-scans have become the prime visualization technique to facilitate its detection. Commonly used by radiologists and surgeons, these digitized sliced volumes allow a rapid or more precise analysis of the brain and the possible anomalies. However, if the visual detection of the tumor can be quickly perceived by any trained eye thanks to the contrast agent, as seen on Figure 2.1, a more-advanced study of the brain tumor and the potential edema to evaluate the type of tumor and

give a prognostic is time consuming.

Image processing then tends to impact the clinical process in distinct phases. First, it helps facilitating the detection and segmentation through machine learning either unsupervised [49,91] or supervised [7,37,86], or through more conventional methods such as active contours [42,88,116], or watershed [73]. Second, machine learning can be used to classify the types of tumor between Glioma, High-grade and Low-grade, and Meningioma [58,95,96], as much as separating the edema from the actual tumor [116]. Finally, a post processing steps allow the surgeons to find the best entry point to either program a biopsy or extract mutated cells [74].

The process remains the same for the blood-vessel segmentation [51,56,103], where this time the applications and the scale variate from sub-millimeters in the eye for example [43,98,100] to arteries feeding directly from the heart, with a diameter of around 2 to 3 centimeters [59,60].

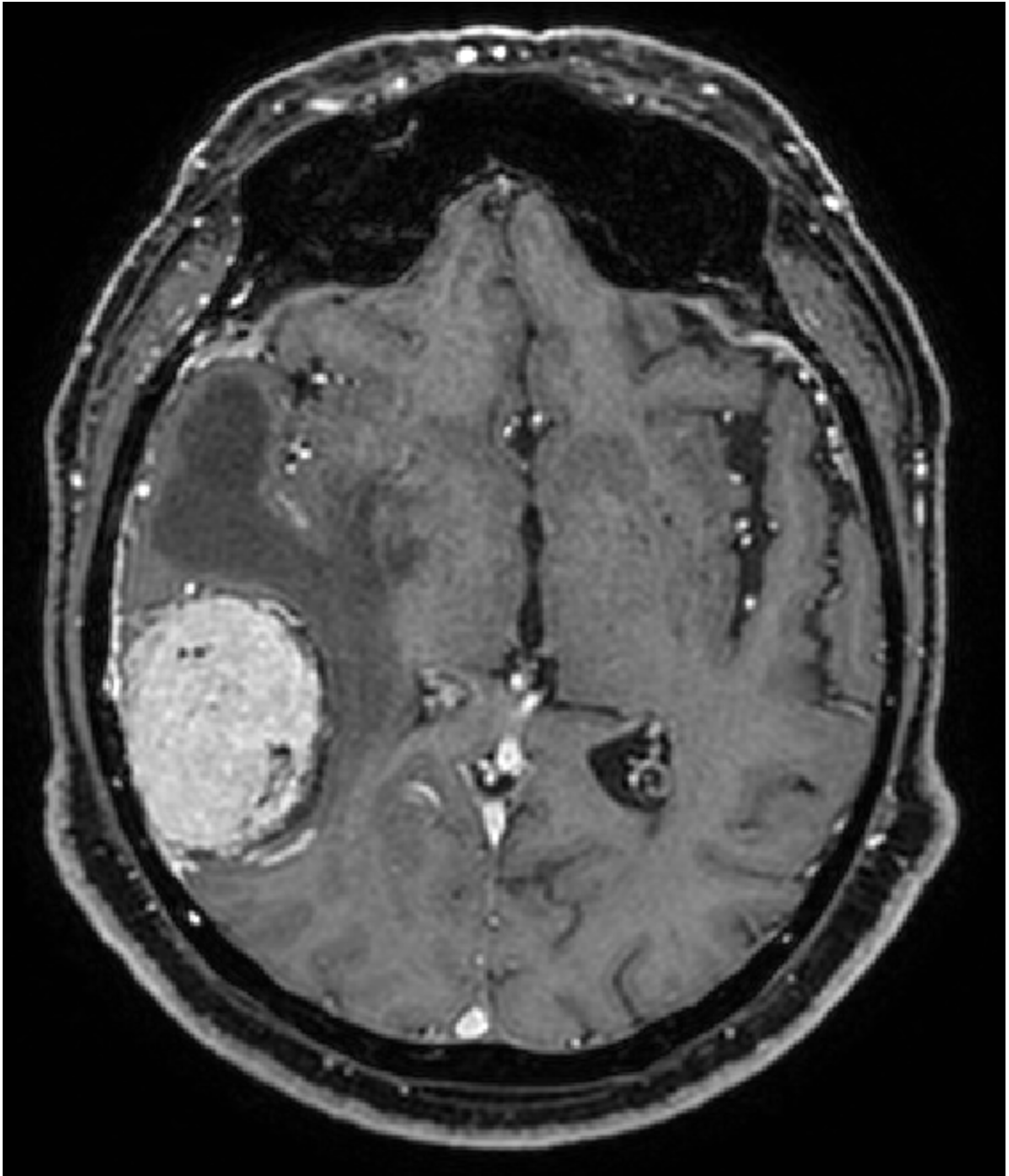


Figure 2.1: Contrasted MR imaging of a patient with a brain tumor: it appears in bright intensity on left side, while the edema results in a darker intensity, surrounding the tumor up and right on the image.

# Chapter 3

## Methods

### 3.1 Overview of the VF approach

In a typical scenario of a procedure performed via a vascular access, a tetherless MRbot is introduced into the vessel at an inlet location  $In(r)$ , for example via an intravascular (IV) cannulation, and maneuvered toward a targeted location  $T(r)$  where  $r$  is the MR coordinate system location. Generation of the guidance cues is based on two criteria: (1) assurance that the MRbot does not harm the vessel (e.g., perforation or rubbing), and (2) accurately reach the targeted anatomy. In this work we made two assumptions. First, all structures are static; this is in a first approximation appropriate to describe the vascular tree in the clinical paradigm of interventions in the brain. However, this is not the case in other organs, for example in the coronary arteries or in the heart blood chambers in which cases the guidance cues are dynamic (for example as shown before in [15,40]). Second, the MRbot size is

such that it can maneuver inside the entire length of the vessel of interest; in practice spherical MRbots can be produced in different sizes (that does have consequences as discussed in Section 5.2 ). Figures 1(a)-1(b) illustrate the proposed approach. The magnetic resonance angiography (MRA) is segmented to generate the vascular tree  $OBJ(1, j)$ . The index  $j$  refers to the digitized form of the MRA 3D vascular path. The centerline  $P(j)$  and a guidance corridor  $GC(j)$  are generated so that the radius  $R_{GC}(j)$  of the  $GC(j)$  is smaller than the diameter  $R_V(j)$  of the segmented structure  $OBJ(1, j)$ . An MRbot can safely maneuver in the 3D cylinder with radius  $R_{GC}(j)$  surrounded by a ring-like safety zone  $S_Z(j) = R_V(j) - R_{GC}(j)$  within which no motion is allowed. The operation of this control scheme can be appreciated considering that the force  $F_G(j)$  applied to the MRbot at location  $j$  has a “forward” propulsion  $F_A$  and a transverse correction component  $F_T$ ; they are synchronously adjusted to keep the MRbot always inside  $GC(j)$  and as close to  $P(j)$  as possible.

## 3.2 Computational framework

In the computational core the 3D vascular path is represented as a  $(6, N_P)$  matrix where  $N_P$  is the digitization number after processing the MRA data: 3 coordinates  $[X(j), Y(j), Z(j)]$  of the centerline point, the radius of the vessels  $R_V(j)$ , the radius of the guidance corridor  $R_{GC}(j)$ , and the curvature  $\kappa(j)$ ; as illustrated in Fig. 2(a) the path is visualized as a linear entity  $[X(j), Y(j), Z(j), R_V(j), R_{GC}(j), \kappa(j)]$ ;  $1 \leq j \leq N_P$ . In the prototype version, the computational core is composed of four task-dedicated software modules, as illustrated in Fig. 3.1. Parameters of the routines are

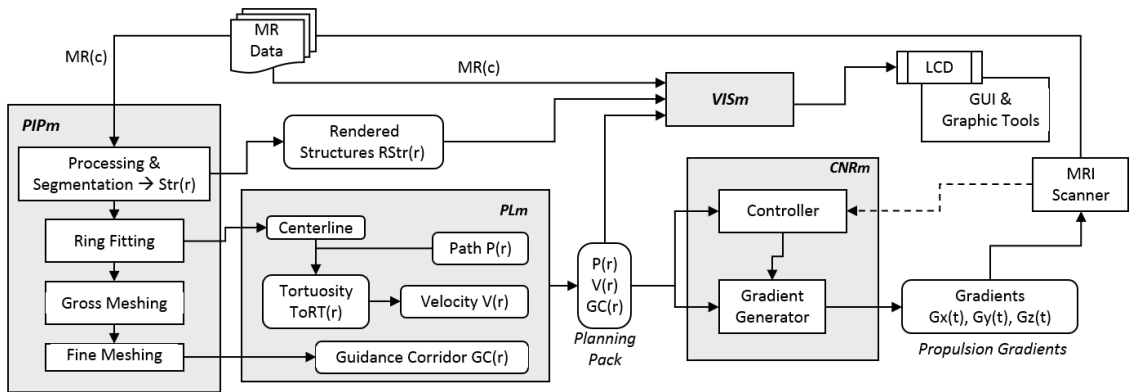


Figure 3.1: Architecture of the core (refer to Table 1 for definitions) of the system depicting processes and data flow paths among them. PIPm: Preoperative imaging processing module; PLm: Planner module; CNRm: control module; VISm: visualization module.

accessible via the graphic tools of the GUI shown on the LCD and/or of a HoloLens.

Table 1 reviews the parameters for ease of reference. In each current form, the core was developed and tested on MATLAB for the flexibility in testing image-based processes; but it does not offer the benefits of C/C++ and associated libraries.

### 3.3 Preoperative imaging processing module

The input to the Preoperative Imaging Processing module (PIPm) are the preoperative MRI data that are processed to render the anatomical structures of interest that will then be used by the Planner and the Visualization modules. Currently, the PIP module includes three routines for segmentation of the tumor, the skin and vessels. Due to the small amount of data we had available, it was decided to use a toolbox approach: building an algorithmic process to perfectly fit only one set of medical

Table 3.1: Data used by the computational core.

Entity	Description	Source	Used by	file
$MR(c)$	MR data	MRI	PIPm, VISm	.dcm
$In(r), T(r)$	Inlet and Target	PIPm		
$\{OBJ(j, r)\}$	Segmented objects	PIPm	VISm	.jpg
$P(j)$	Path	PLm	CNRm VISm	(*)
$GC(j)$	Guidance corridor	PLm	CNRm, VISm	.srt
$\kappa(j)$	Curvature	PLm	CNRm	(*)
$V(j)$	Velocity profile	PLm	CNRm VISm	(*)
$G(r, t)$	Gradient waveform	CNRm	MRI	
PIPm: Preoperative Imaging Processing module; PLm: Planner module; CNRm: control module; VISm: visualization module; (*) elements of the matrix.				

data is bound to fail. In fact, the same way a machine-learning method can overfit, the method created will behave as expected for the data set it was built for but will have more chances to misbehave as new data sets are added. This can be due to various external parameters, such as the unique anatomy of each patient, the intrinsic imaging value of the MR-scanners or even the timing at which the contrast agent is injected. A partial solution is thus to create a toolbox of segmentation algorithms that can be used interactively, allowing the surgeon or medical personnel to quickly extract the desired region: tumor, vascular tree, and skin.

As discussed in Section 6 and to better fit the final desired system, this set of computing tools will be improved to match the model of the MR-scanner to which it will be attached to, but to keep the versatility and interactivity of the current version.

*Extraction of Tumor:* The tumor,  $OBJ(1, r)$ , was extracted from the multislice set of Post-Contrast T1-weighted Fast Field Echo (post-T1FFE). A region-growing algorithm was manually seeded by creating a few polygons inside the tumor. The tumor was then segmented based on the criterion introduced by Pohle et al. in [80]: at step  $t$ , all voxels connected to the existing region  $R(t - 1)$  are added to  $R(t)$  if their value is included in  $I(t)$  where:

$$I(t) = [v - \alpha \cdot \sigma^-; v + \alpha \cdot \sigma^+] \quad (3.1)$$

with  $v$  being the median of all the values of the voxels included in  $R(t - 1)$ ,  $\alpha$  a user-selected parameter set visually,  $\sigma^+$  the standard deviation of the values of  $R(t - 1)$  that are greater than  $v$  and  $\sigma^-$  the standard deviation of the values of  $R(t - 1)$  that are lower than  $V$ . Two voxels are connected if they have at least one vertex in common.

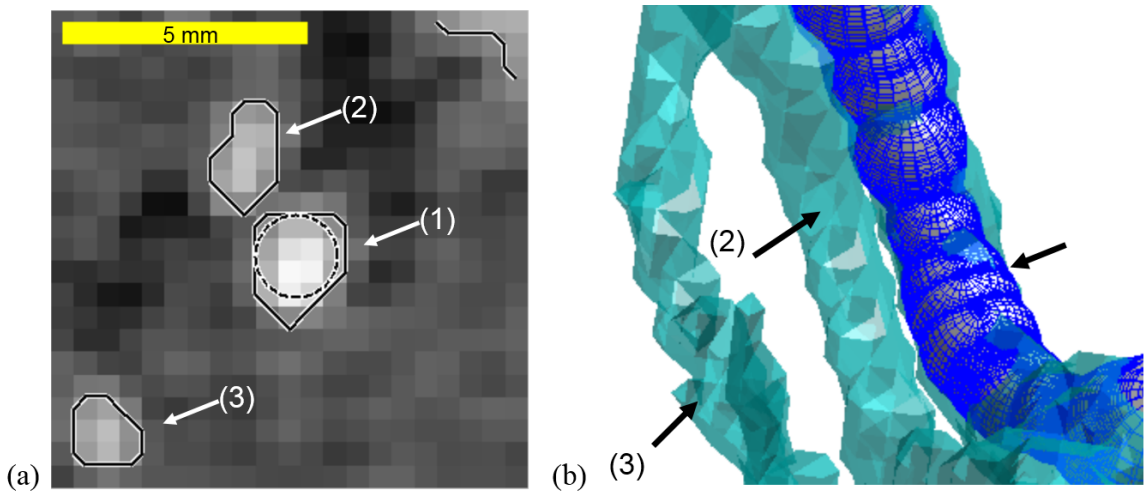


Figure 3.2: Representative input and output data of the PIPm showing a zoomed in area of the original DICOM image (95th slice of the TOF-MRA set that depicts three cerebral vessels (1)-(3)). The solid line is the output of the PIPm segmentation and the dashed circle is the maximum CG circle for vessel (1). Vessel (1) is the one that reaches the lesion and inside which the MRbot maneuvers. (b) Output of the PLm showing the segmented vessels and the CG mesh for vessel (1); this output is sent to the CNRm and VISm. No smoothing or interpolation was used, clearly demonstrating the challenge with native limited resolution of MR data.

Upon completion of the region growth step, the surface is smoothed using a morphological closing with a sphere mask to erase small gaps due to noise. In our case, an  $\alpha$  of 1.5 allowed us to segment the tumor.

*Extraction of Blood Vessels:* Arteries  $OBJ(2, r)$  were extracted from the multislice set of Time Of Flight (TOF) magnetic resonance angiography (MRA). Segmentation was based on a simple signal intensity high-pass filtering algorithm, i.e., thresholding. Two combined manual thresholds were used: the first was directly applied on the value of the voxels, while the second used the results of the Frangi filter to allow finer vessels to appear [31]. The filter allows the user to be less restrictive when applying the threshold on the value of the voxels by favoring the detected tubular structures. Once the thresholds are visually set, various segmented volumes corresponding to the wanted artery trees were selected, hence cutting any unwanted noise that passed through both thresholds. The Frangi filter was used on different scales  $s$  ranging from 0.3 to 5. For extracting vessels there are many superior methods. However, we selected the simple filter-based approach because the next stage of this framework will have to run in real-time using a customized TOF sequences.

*Extraction of Skin:* The skin was extracted primarily for visualization purposes, as proposed by our collaborating neurosurgeons. It generates two skins,  $OBJ(3, r)$  and  $OBJ(4, r)$ , one from the TOF MRA and the other from the post-contrast T1w-FFE, as shown in Fig. 3.4, that can be used in case the patient moved during the scanning process to register the different MR data sets; this was not needed in the two studies we processed. In either data set, skin extraction entailed the following steps. First, a threshold was visually applied to the image stack, segmenting at best

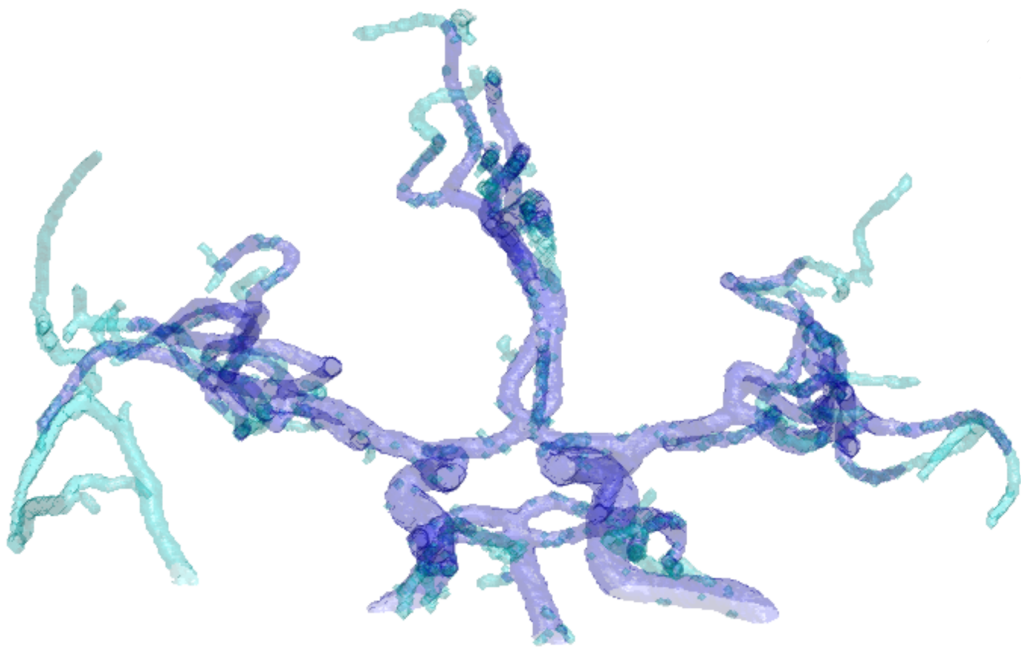


Figure 3.3: Comparison between the manual results obtained without (in blue) and with the help of the Frangi filter (in cyan)

the whole visible skin. Then, a morphological closing was applied using a spherical mask to eliminate the segmented Rician distributed noise surrounding the skin [36]. The noise here does not need to be completely eliminated through more extensive filtering as the skin is used as a visual marker for the surgeons. Thus, the radius of the mask sphere is high enough to hide the noise. The operators have access to set the parameters in the PIPm routines, such as the thresholds in region growing and the Frangi filter.

### 3.4 Planner module

The input to Planner module (PLm) is the segmented vascular tree  $OBJ(2, r)$  that is processed by the following three routines that upload their corresponding outputs to the data pipeline: (1) extraction of path  $P(r)$ , (2) generation of guidance corridor  $GC(r)$ , and (3) generation of velocity profile  $V(r)$ , where  $r$  is the MR coordinate system location (onto which all entities of the AoP are inherently co-registered). These tasks are: Extraction of Path  $P(r)$ : A first path approximation, between the inlet and the target, is generated from the previously extracted artery volumes as 26-connected graphs: each voxel is connected by two unilateral edges to its 26 neighbors. The weight of each incoming edge to the voxel  $v$  is the input to the energy function  $E(v)$ . The path is then the shortest one from the inlet to the target voxel, calculated using Dijkstra’s algorithm. In this work, the energy function was:

$$E(v) = \exp \left\{ \max_{u \in A} (d(u) - d(v)) \right\}, \quad (3.2)$$

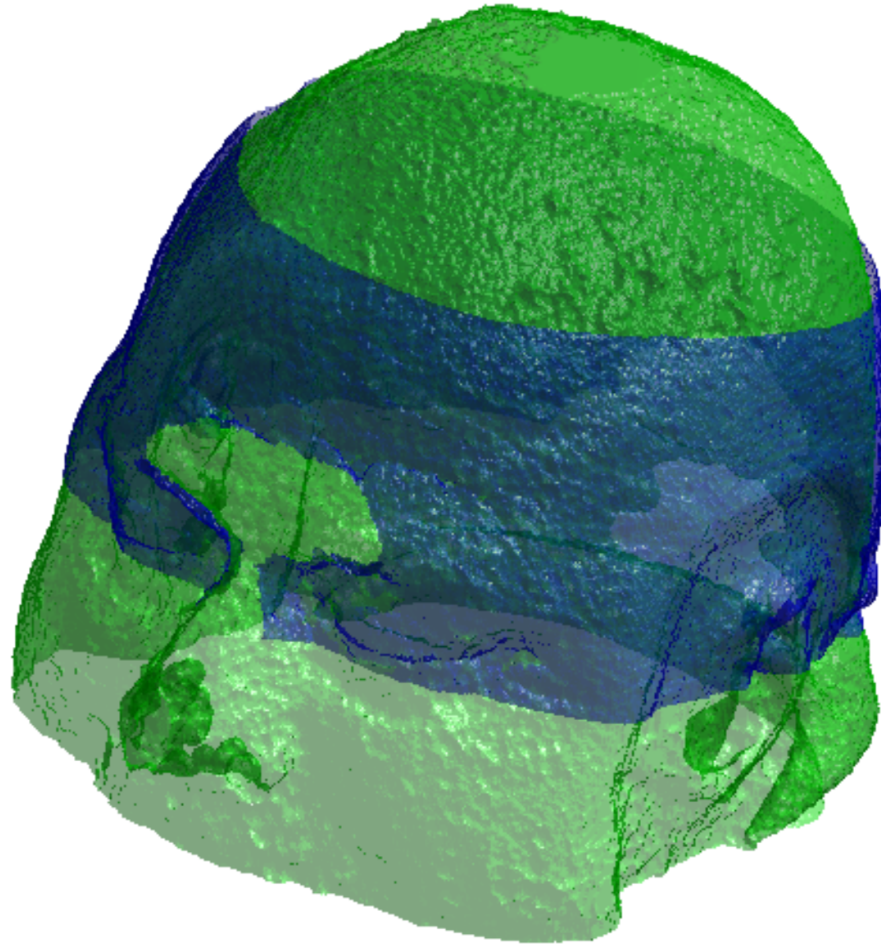


Figure 3.4: Registered skin from both the TOF MRA scan in blue and the post-contrast T1w-FFE scan in green.

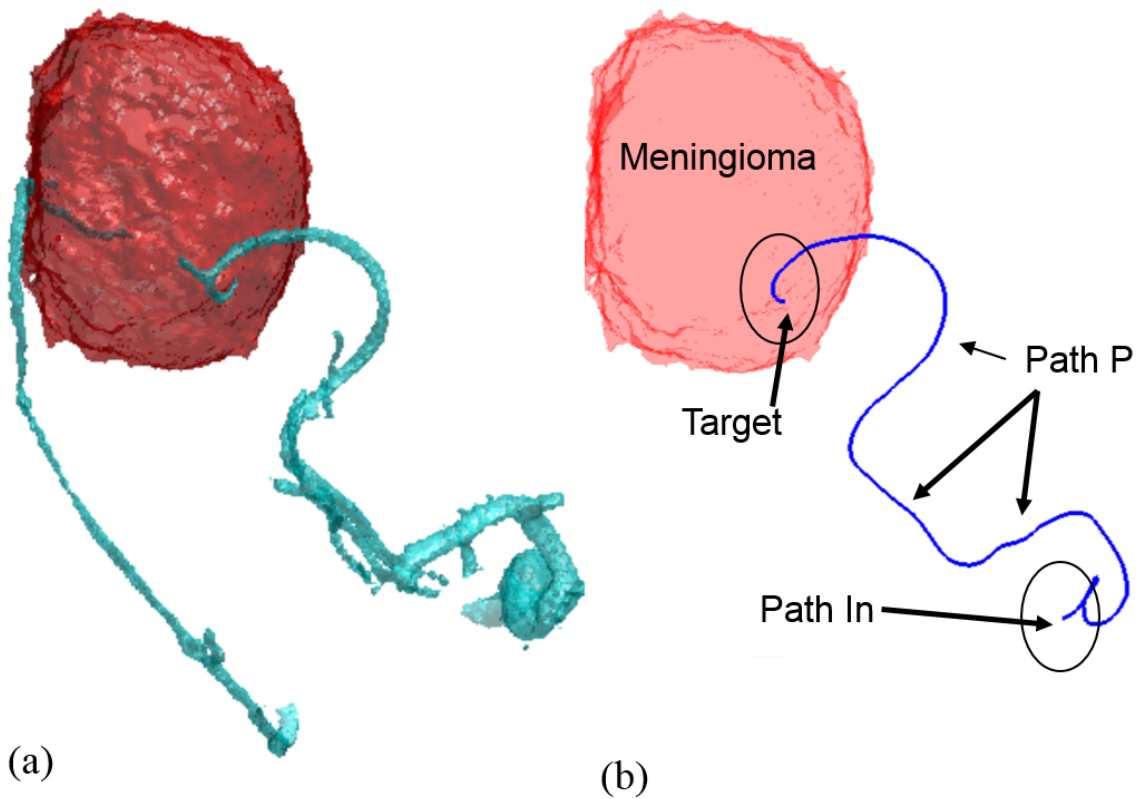


Figure 3.5: (a-b) 3D scene showing (a) 3D rendered vessels and meningioma and (b) the extracted path  $P(r)$  from the inlet to the targeted sites. All 3D structures are inherently registered and scaled to the MR scanner coordinate system. No smoothing or interpolation was used.

where  $A$  is the set of segmented voxel in the artery tree and  $d(v)$  is the distance from the voxel  $v$  to the closest voxel in the matrix not in  $A$ . This energy function was selected so the generated path approximates the center-line of the vessel and forces the shortest path through bifurcations and other imperfections along the arteries. Figure 3.6 shows the difference between our path and the geometrical center-line on a manufactured volume. The center-line is found using the 3D Voronoi diagram of the surfaces voxels: each vertex of the diagram is considered a node in a graph and is connected to the other vertices of the cells it belongs to, if and only if they are on the same surface. Thus, two vertices of the same cell are not neighbors if the line joining them goes through the convex hull of the cell. Each Voronoi cell is a convex volume. We use Dijkstra's algorithm on this graph, but this time using the following energy:

$$E_2(v) = \frac{1}{d(v)} \quad (3.3)$$

The search is restricted to the vertices inside the volume of the vascular tree and each point of the center-line is the furthest from the surface due to the diagram nature.

The path generated is situated in the matrix system, which does not take into account the position of each voxel in the Reference Coordinate System (RCS). To correct this, the path is first translated into the RCS using the DICOM information present in the header of the MRI slices: the position of each slice, and the pixel size in each slice. The same is done for a narrow band  $B$  of voxels around the set  $A$  found earlier.  $B$  is found by dilating  $A$  using a  $3 \times 3$  voxel cube and then subtracting  $A$ :  $B$  is thus the first 6-connected layer of voxels surrounding  $A$ . Two voxels are 6-connected if they have at least one face in common.

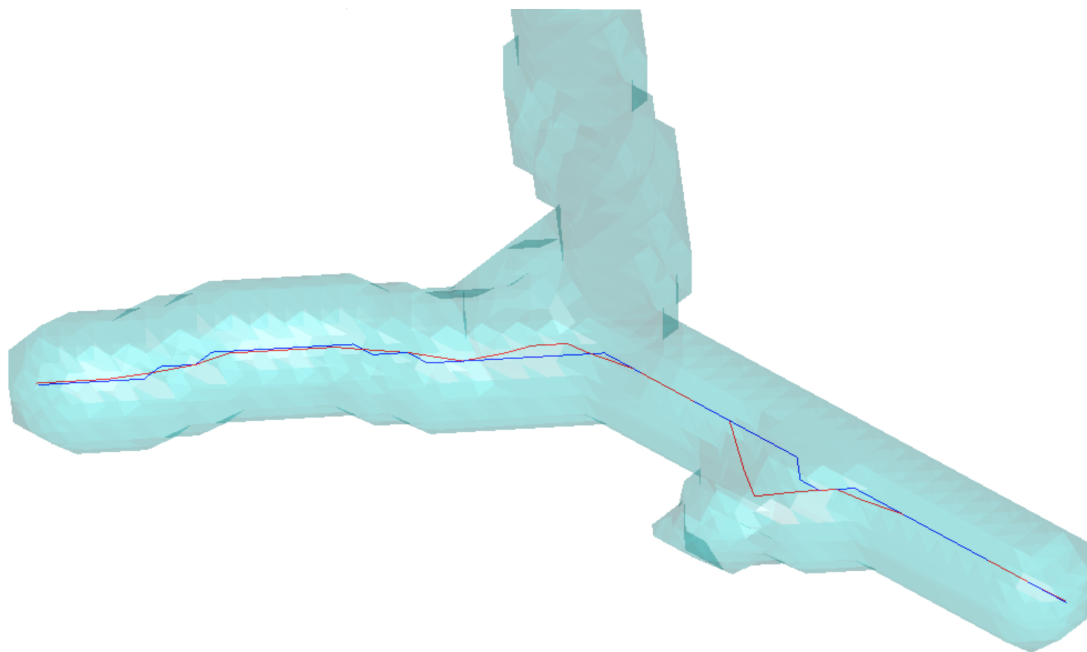


Figure 3.6: Comparison of deformation due to imperfection between the shortest-path algorithm in blue, and the geometrical center-line in red.

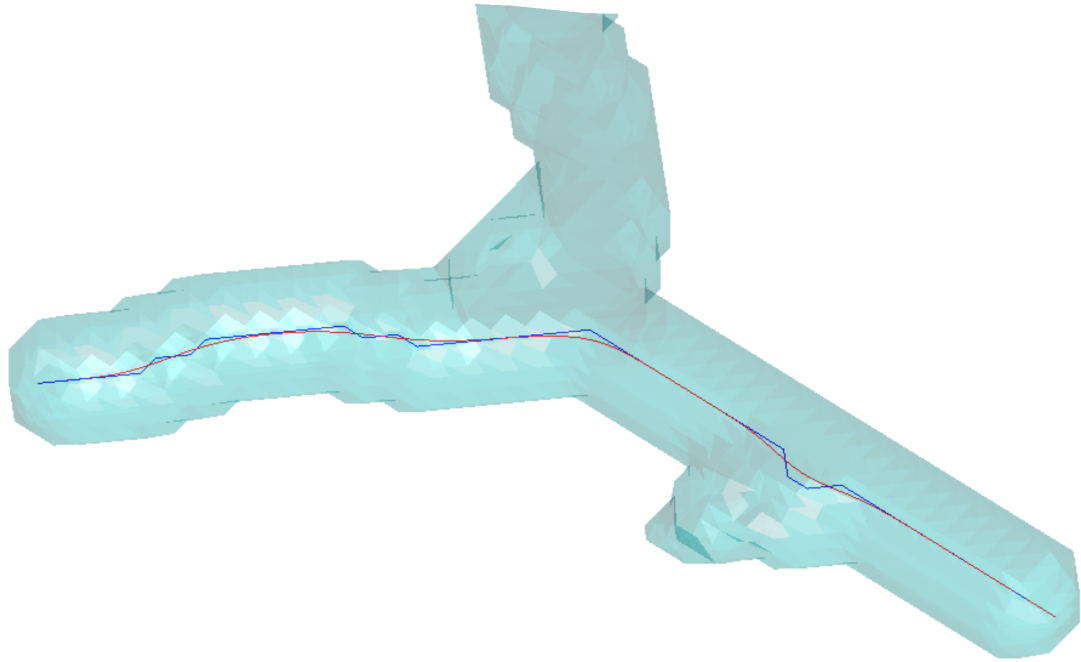


Figure 3.7: Comparison between the original path in blue and the generated corrected path using the b-spline in red.

*Generation of Guidance Corridor(s):* The path given by Dijkstra's algorithm is restricted to the voxels themselves and may thus have sharp turns or may contain saw-like parts. The first step following the RCS translation is then to smooth the path by approximating it with a high-order B-spline as shown in Figure 3.7. Finally, the radius of the tube is the distance between the points of the B-spline and the closest point in B. The result is a set of points representing a path along with a radius value describing a corridor that can be used as a virtual fixture. This corridor can then be reduced, either using a constant safety margin, or a percentage of the initial corridor to create the safety guidance corridor ensuring that any object going through will not touch the inner walls of the vessels.

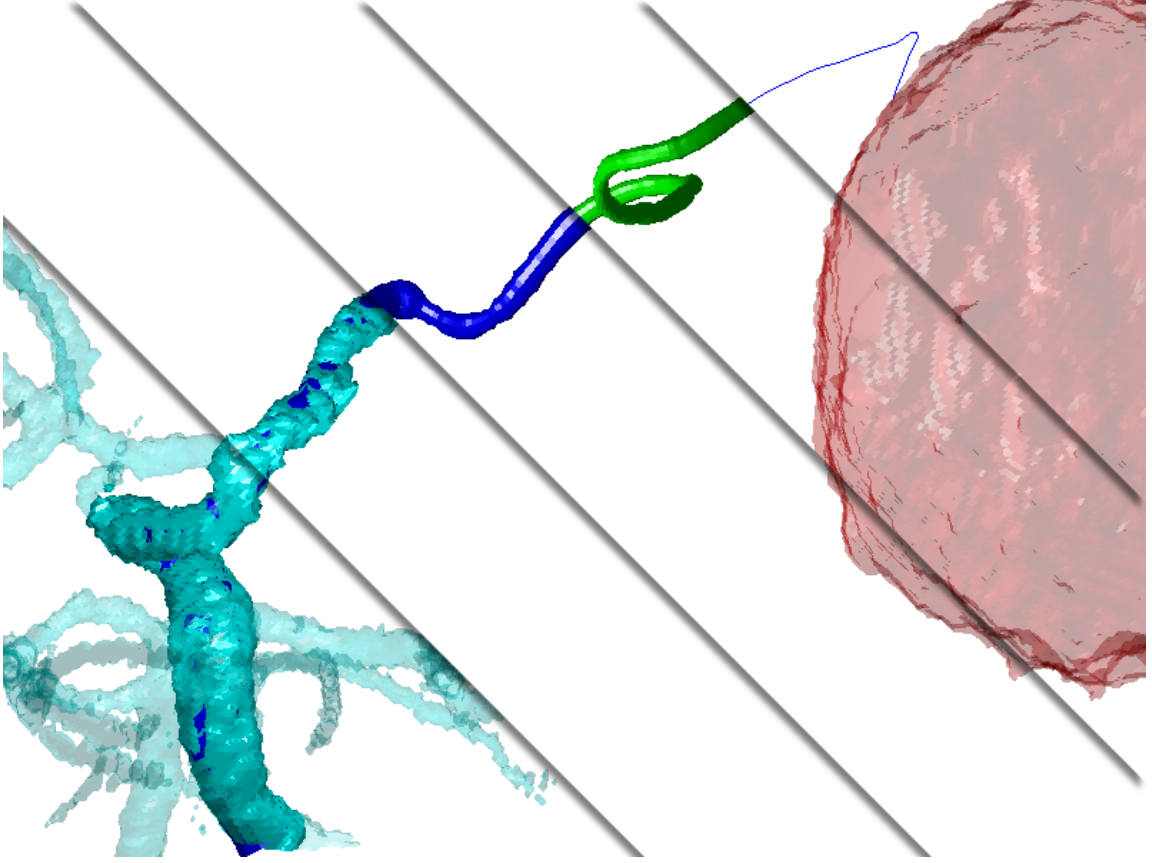


Figure 3.8: Image showing the different layers of the path planning. From bottom left to top right: Vascular tree, feeding artery, tube, safety corridor, path

*Generation of velocity profile:* This routine generates a targeted velocity profile  $V(r)$  along the path  $P(r)$ , calculating its vector for each one of the points of the path.  $V(r)$  is assigned to zero at  $In(r)$  and  $T(r)$  while for any other location  $V(r)$  is calculated with:

$$V(r) = \frac{V_0}{1 + \kappa(r)/\kappa_0} \cdot \frac{R_s - R_{GC}(r)}{R_0} \quad (3.4)$$

where  $R_s$  is the radius of the MRbot and  $V_0$ ,  $\kappa_0$  and  $R_0$  are constants allowing to adjust the velocity profile.

### 3.5 Control module

The controller performs a control of the velocity  $\mathbf{V}_s$  of the MRbot as well as its position  $\mathbf{P}_s$ . A setpoint needs to be generated first. The point of  $\mathbf{P}(r)$  that is the closest to  $\mathbf{P}_s$  is selected. This point (denoted  $\mathbf{P}_c$ ) is taken as the reference point. The desired velocity at this point is  $\mathbf{V}_c$ . Errors on the position and velocity can be calculated with:

$$Position\_error = |\mathbf{P}_s - \mathbf{P}_c| \quad (3.5)$$

$$Velocity\_error = |\mathbf{V}_s - \mathbf{V}_c| \quad (3.6)$$

A block diagram of the controller is presented in Figure 3.9. The controller is composed of a PID regulator and a feedforward component that directly outputs the optimal control. The optimal control  $F_{opt}$  corresponds to the gradient that allows compensating for the drag produced by the blood on the sphere:

$$F_{opt} = \frac{1}{2} \cdot C_d \cdot \rho \cdot A \cdot |\mathbf{V}_{blood} - \mathbf{V}_c| \quad (3.7)$$

with  $C_d$  being the drag coefficient,  $\rho$  the density of blood (1025 Kg/m<sup>3</sup>),  $A$  the reference area and  $\mathbf{V}_{blood}$  the blood velocity vector.

The PID regulator takes as input the sum of the velocity error and the position error. The position error is multiplied by a coefficient  $k$  that sets the importance of the position control with respect to the velocity control. In a practical application, the velocity can be obtained from the position measurement by using a Kalman filter.

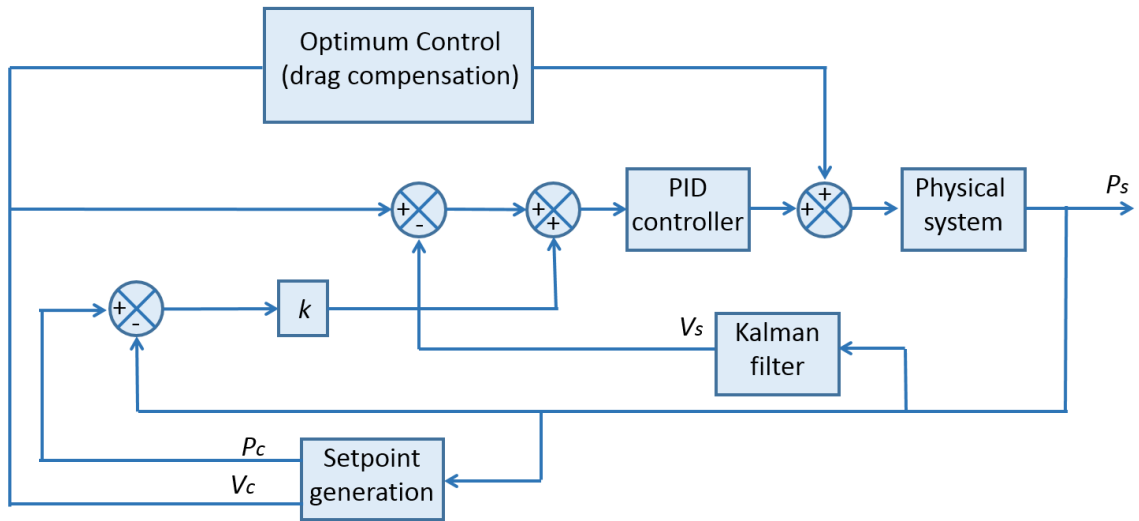


Figure 3.9: Diagram presenting the architecture of the trajectory controller.

### 3.6 Visualization module

The purpose of the Visualization module (VISm) is to generate and update a virtual reality environment that simulates the Area of the Procedure (AoP). The VISm can display any combinations of the following objects: MR images, the segmentation contours, the 3D guidance corridor GC, and/or the current position of the sphere while a simulation is running. All objects in the AoP are registered and scaled to the coordinate system of the MR scanner, which offers a natural space of visualizing 3D geometric structures. The update rate of the AoP is the same as that of the simulation, and if rt-MRI is used, it is the rate of MR data collection [15, 77]. The AoP can be accessed by a HoloLens that polls the Host PC for updated versions of the virtual scene.

# Chapter 4

## Algorithms

In this section are presented the main algorithms used in the PIP module, the PL module, as well as the Control module.

### 4.1 PIP module – Region-Growing algorithm

The Region-Growing algorithm takes as input three parameters:

- The volume data  $D$ , an  $n \times m \times o$  matrix of values
- The initialization region  $I$ , an  $n \times m \times o$  boolean matrix where *true* represents the seeding region
- The criterion  $C$ , a function  $C(S, v)$ 
  - taking a set of value  $S$  and the value of a voxel  $v$  as input

- returning *true* if the voxel fits the criterion over the values of  $S$ .

Let  $A$  be a generic matrix. Let  $p$  be a voxel within the boundaries of  $A$ ,  $A(p)$  is the value of  $A$  at the voxel  $p$  location. The result of this algorithm is the grown region

**Data:** Data  $D$ , Initialization  $I$ , Criterion  $C$

**Result:**  $n \times m \times o$  boolean matrix

Let  $R$  be  $I$ ;

**repeat**

    Let  $S = \{D(p) \mid I(p) \text{ is } true\}$  ;

$Q \leftarrow R$  ;

**foreach** *Voxel  $n$   $k$ -connected to  $R$*  **do**

**if**  $C(S, D(n))$  **then**

$D(n) \leftarrow true$  ;

**end**

**end**

$R \leftarrow Q$  ;

**until**  $R$  has stopped growing;

**Algorithm 1:** Region-growing algorithm

produced by the seed and criterion: it is an  $n \times m \times o$  boolean matrix where *true* represents the inside of the region.

## 4.2 PL module – Dijkstra’s algorithm

Dijkstra’s algorithm or Fast Marching Method in our case, takes four parameters as input:

- The graph  $Gr$  and respective energy  $E$  of the edges per node. In our case, we simply use the 3D morphology of the matrix to define the  $k$ -connected

neighbors for the path, or the set of cells and respective vertices for the Voronoi center-line.

- The entry node  $v_{in}$  being the closest  $Gr$  node to  $In(r)$  shown in Table 3.1
- A list of  $n_{out}$  exit nodes  $V_{out}$ . In this case,  $n_{out} = 1$  and  $V_{out}$  contains only the closest  $Gr$  node to  $T(r)$  shown in Table 3.1.

Let  $L_{min}$  be an adapted sorting data-structure that will contain a ascending list of energy. Inserting an element into  $L_{min}$  returns the index  $i$  to which position this new element was inserted.

Internally, we change the structure of  $Gr$  so it can contain a status *visited* or not, and a *parent* linking to another node of  $Gr$ . The parent can be empty. This algorithm returns a set of  $n_{out}$  *path*  $P$  in a form of an ordered list of nodes: each path can have a different number of nodes, as the exit nodes in  $V_{out}$  are not at the same distance from the inlet  $v_{in}$ .

**Data:** Graph  $Gr$ , energy  $E$ , inlet  $v_{in}$ , targets  $V_{out}$   
**Result:** a set of  $n \leq n_{out}$  paths from  $v_{in}$  to each reachable vertices of  $V_{out}$   
Let  $L_v = \{v_{in}\}$  the list of vertex to expand from;  
Change  $Gr(v_{in})$  status as *visited*;  
Initialize all the parents in  $Gr$  as  $\emptyset$ ;  
Insert the energy 0 of  $v_{in}$  into the previously empty  $L_{min}$ ;  
**while**  $\exists v \in V_{out}$  such as the parent in  $Gr(v) = \emptyset$  **AND**  $L_{min} \neq \emptyset$  **do**  
    Let  $v$  be the first element of  $L_v$ . It is removed from  $L_v$ ;  
    Let  $e$  the first value of  $L_{min}$ . It is removed from  $L_{min}$ ;  
    **foreach** Node  $u$  connected to  $v$  in  $Gr$  **AND** not yet visited **do**  
        Insert  $e + E(u)$  in  $L_{min}$ . It is inserted in ascending order at index  $i$ ;  
        Insert  $u$  in  $L_v$  at index  $i$ ;  
        Change  $Gr(u)$  status as *visited*;  
        Change  $Gr(u)$  parent as  $v$ ;  
    **end**  
**end**  
**foreach** Node  $v_{out}$  in  $V_{out}$  **do**  
    Let  $P_{v_{out}}$  the path associated with  $v_{out}$ ;  
    Let  $u = v_{out}$ ;  
    **while**  $Gr(u)$  parent is not  $\emptyset$  **do**  
        Add  $u$  at the end of  $P_{v_{out}}$ ;  
        Let  $u$  be its parent;  
    **end**  
    Inverse the order of the path;  
**end**

**Algorithm 2:** Pseudocode of the path finding algorithm

### 4.3 Control module

The trajectory controller algorithm takes as input the various parameters, such as the patient's anatomy, the sphere parameters, the MRI machine parameters, and the planned path. The output of this algorithm is:

**Data:** The planned path, environment parameters  
**Result:** A timeline of gradients amplitude needed to actuate the sphere  
**while** *Procedure is ongoing* **do**  
    Get  $\mathbf{P}_s$  and  $\mathbf{V}_s$ ;  
    Search  $j_c$  such as  $|\mathbf{P}_s(j_c) - \mathbf{P}(j_c)| = \textit{minimum}$ ;  
    Calculate the inputs to the PID regulator;  
    Calculate the output from the PID regulator;  
    Calculate the optimum control;  
    Calculate and update the output of the controller;  
**end**

**Algorithm 3:** Pseudocode of the trajectory controller.

- In case of the simulation: a step-by-step 3D gradient  $G(t)$  array where each step happens  $\delta t$  after the previous one. The result is then an array of vectors defined for an integer  $k = 0$  to the number of steps it took to reach the target, such as the vector at index  $k$  represents  $G(k\delta t)$ .
- In case of the live procedure, the algorithm will output in real-time  $t$  the gradient  $G(t)$  to use to actuate the sphere inside the vascular tree.

# Chapter 5

## Modelization, simulation, and results

### 5.1 Modelization of the physical system

The force applied to the ferromagnetic sphere is proportional to its magnetization (5.1). The magnetic field  $B_0$  of an MRI machine is strong enough to saturate steel magnetically. The magnetization of the sphere was thus considered to be constant and equal to the maximum magnetization steel can have. The saturation flux density of 4750 steel is approximately 1.6 T which is equivalent to a magnetization  $M$  of  $1.27E^6$  A/m. The force vector applied on the sphere  $\mathbf{F}_s$  is calculated using eq. 5.1,  $\mathbf{G}$  being the gradient vector and  $Vol$  the volume of the sphere.

$$\mathbf{F}_s = \mathbf{G} \cdot M \cdot Vol \quad (5.1)$$

The modelization of the field produced by the MRI scanner is straightforward. MRI scanners produce almost uniform gradients inside the uniformity sphere. The gradient is therefore considered to be constant in the model.

The drag produced by the blood on the sphere was included in the model. It was assumed that the flow is separated, i.e., the drag is proportional to the square of the relative speed. The drag coefficient  $C_d$  of a sphere is equal to 0.47 for a Reynolds number equal to  $10^4$ . The drag can be calculated with eq. 5.2. This equation is similar to eq. 3.7, except that the velocity of the sphere  $\mathbf{V}_s$  is used in place of the velocity setpoint  $\mathbf{V}_c$  that was used to calculate the optimal control. It was assumed that the blood flows at a constant velocity  $\mathbf{V}_{blood}$  equal to 1 mm/s and that the flow is collinear to  $P(r)$ . See equation 3.7 for  $C_p$ ,  $\rho$  and  $A$  notation.

$$F_{drag} = \frac{1}{2} \cdot C_d \cdot \rho \cdot A \cdot |\mathbf{V}_{blood} - \mathbf{V}_s| \quad (5.2)$$

## 5.2 Simulation Results

The model and the controller were implemented in MATLAB. Results of simulations are presented in Fig. 5.1 and 5.2. The parameters used for the PID controller are  $K_p=0.3$ ,  $K_i=0.2$  and  $K_d=0.01$ . The constant  $k$  weighting the regulation of the

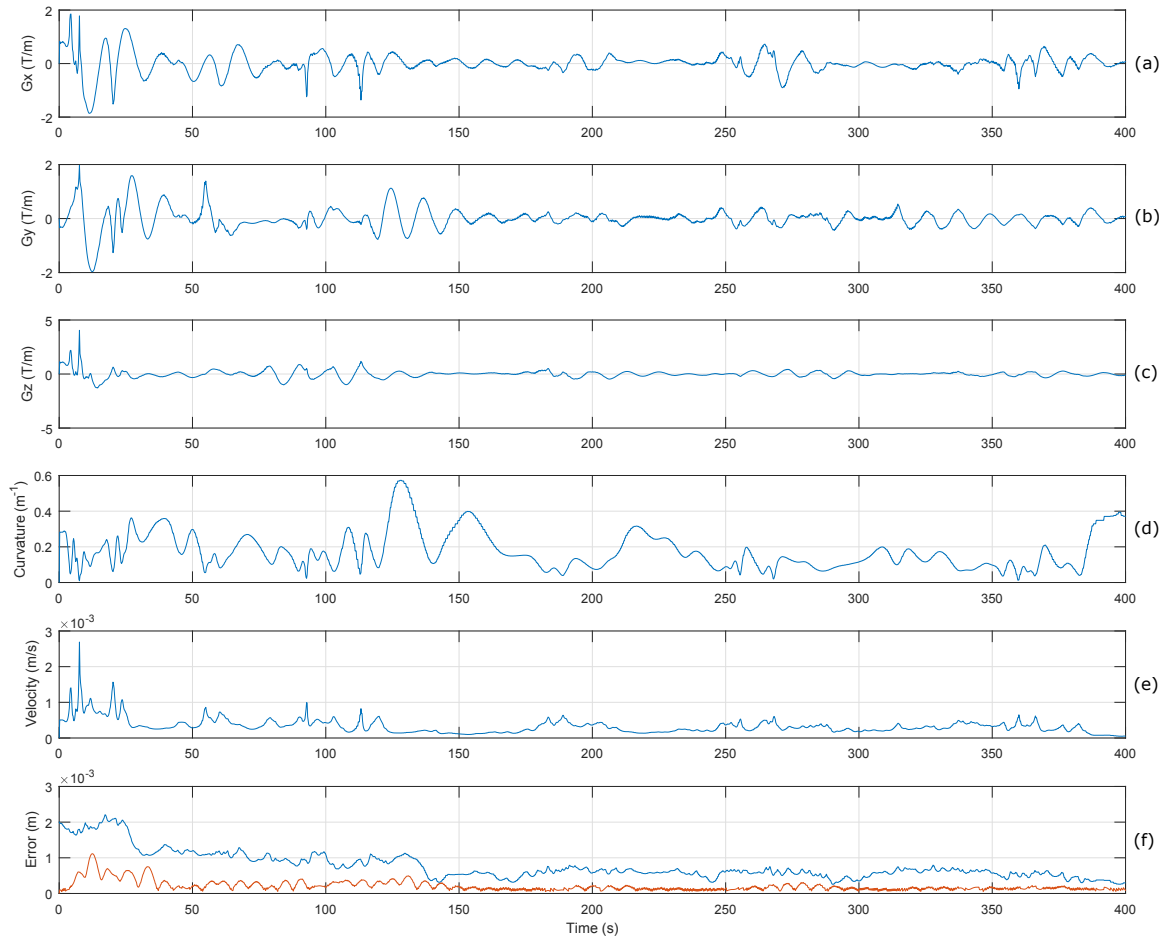


Figure 5.1: Results of the simulation of the system. (a), (b) and (c) present the gradients generated by the MRI scanner for each axis. (d) is a plot of the curvature of the path. (e) shows the velocity of the MRbot and (f) compares the positioning error (red curve) with the maximum acceptable error (blue curve). The sphere is inside the guidance corridor when the red curve is below the blue curve. The MRbot stays in the corridor during the complete navigation.

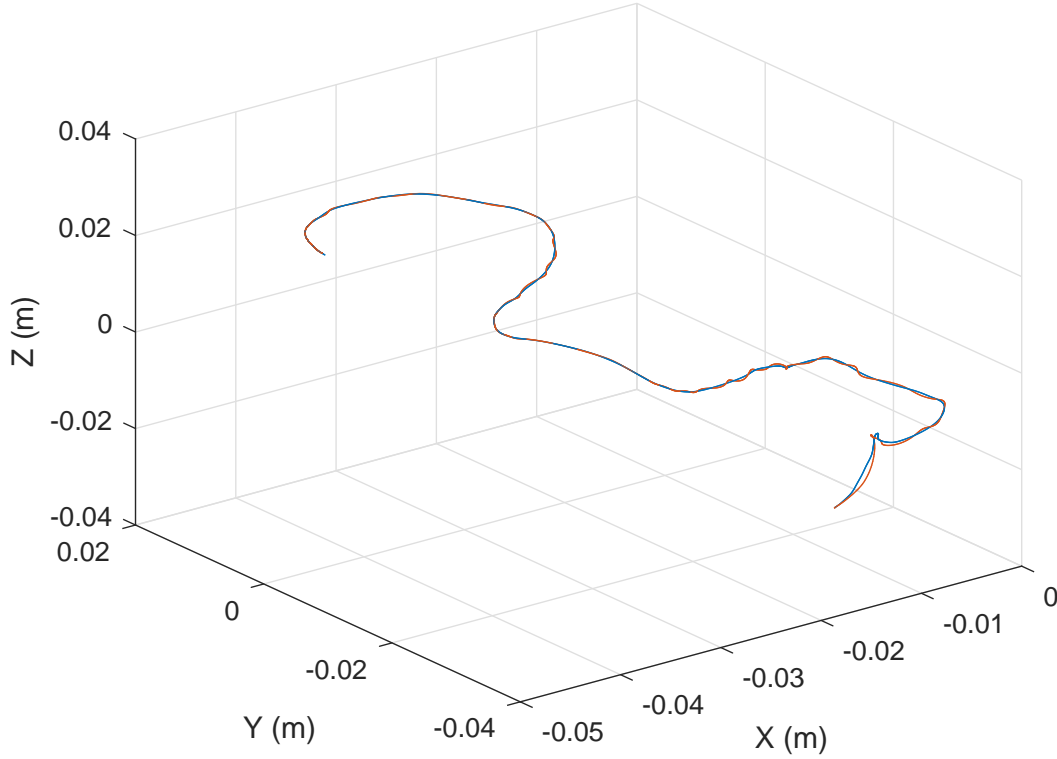


Figure 5.2: 3D plot of the trajectory of the sphere. The graph shows the planned trajectory  $P(r)$  (blue line) and the actual trajectory (red line).

position is equal to 0.3 and allows us to prioritize the control over the velocity rather than the position. In the case of a closed-loop control where the surgeon supervises the procedure with a haptic device, the slow speed of the sphere will allow ample correction time from the operator in detected problematic sections (intersection, sharp turns, etc). This constant factor will be subject to changes depending on the simulation desired and will be tuned more finely once more data is acquired. The diameter of the sphere was 0.6 mm.

As shown in Fig. 5.2, the sphere closely follows the planned path. It is slightly

off the centerline at the beginning of navigation. There, the vessel is large enough to tolerate a few millimeters of positioning error. The PLm thus automatically increased the velocity of the MRbot in this area (see Fig. 5.1 (e)). The curvature of the trajectory (see Fig. 5.1 (d)) also affects the planned velocity (see Section 3.4). A plot of the error on the position of the sphere is shown in Fig. 5.1 (f). The maximum tolerable error corresponds to the radius of the safety corridor minus the radius of the sphere. The sphere is within the error tolerance during the complete trajectory.

To increase the tolerable error, a smaller sphere can be used. However, when the sphere becomes smaller, the gradient needs to increase to produce enough force to move the sphere. With a sphere having a diameter of 0.6 mm like in the presented simulations, the gradient needs to reach a value of 4.05 T/m. This value is larger than the gradient produced by current commercial MRI scanners which are usually limited to values below 0.02 T/m.

# Chapter 6

## Conclusion

MRI actuated and guided MRbots, as carriers of therapeutic agents or even as miniature intervention effectors, are a highly promising area in the field of interventional medicine. In addition they are an intriguing platform to develop new approaches in visual servoing, intelligent sensor control and integrating sensing and control in the same entity (the MR scanner). However, the potential impact and fate of this technology will be addressed in the field: in vivo animal studies and, eventually, human trials. Identification of meritorious clinical paradigms and appropriate evolution of this robotic technology is of paramount importance. As an alternative to catheter based interventions, maneuvering inside the cerebral vasculature to deliver an intervention is an area with potentially high merit. This work is a first step toward assessing the feasibility of such procedures and implementing computational framework for such procedures with emphasis of how to use the pre-operative MRI data. Two primary novel features of this framework were the implementation of MRI-based

virtual guidance cues and the inclusion of a trajectory-based velocity profile. The virtual guidance corridor defined a safety zone within the vessel that was then used for visual inspection and identification of areas along the path of potential safety concern (i.e., the MRbot was coming close to the vessel wall). The velocity profile used a simple approach encountered in mobile robots: the speed is reduced locally when the curvature of the path is high. This provided an additional parametric control for optimizing and modifying anatomy-based motion profiles.

The described prototype version of the computational framework was evaluated for *in silico* simulation of accessing a brain meningioma via the tortuous vessels of the cerebral vasculature. The velocity was adjusted during the navigation as a function of the local curvature and the radius of the guidance corridor. The PID regulator had therefore more time to correct and stabilize the trajectory when in more tortuous segments of the vessel, ensuring that the MRbot remained within the guidance corridor.

The simulations further revealed that the procedure (i.e., MRbot dimensions and velocity profile) can be adjusted, for example, increasing velocity and/or decreasing the MRbot ferromagnetic mass require higher strength gradients to execute the maneuver. In the particular clinical paradigm, the smallest vessel was 0.7 mm diameter, and thus a 0.6 mm diameter MRbot was used. When this small entity was moved with a maximum velocity of 2.8 mm/s, the calculated control from the simulation module required a maximum gradient strength of 4 T/m. This is significantly larger than the gradient currently available in commercial MRI scanners (0.02 T/m). For this particular paradigm, possible solutions are (i) to reduce the speed of the MRbot

and/or (ii) make the MRBot with higher magnetization saturation material (such as Holmium, rather than steel), (iii) incorporate special gradient inserts.

The described work has certain limitations. First, the system was not connected and tested on-line with an MRI scanner. As a consequence, rt-MRI was not included for MRbot tracking and on-the-fly imaging of the path forward to its motion. This is a work-in-progress based on prior work in MRbot [1, 25, 26], on-the-fly-control of the MRI scanner by the control software of a robot [16], and fast MR-sensing with modified k-space trajectories [68]. Second, the core was implemented on MATLAB for streamlining development, testing and processing the output; however, MATLAB is slow and memory-management is inefficient for running such a system. Upon completion of its development, the code will be converted to C/C++, incorporating appropriate libraries (e.g., ITK/VTK/OpenGL), and optimized as we did before with multithread implementation [75] and GPU acceleration [47]. In that previous work on dynamic VF extracted from MRI for cardiac interventions, the code for the generation of 4D guidance corridors was refreshed with a delay of less than 0.50 ms [75]. In that work it was also recognized that the bottleneck was the speed of MRI collection. We expect that, if appropriate MR pulse sequences are developed, the system can run the MRbots with virtually no latency at the computational core level. Third, the control module (CNRm) used a constant blood flow. A future version is planned to include a numerical approach in modeling flow [38]. Moreover, the material used to build such sphere needs to be magnetically susceptible enough and have a high magnetization saturation to be driven by the MR machine, while remaining safe for injection into the patient's blood stream. Finally, we selected

certain algorithms for processing the preoperative data in the PIPm. Although many other algorithms exist, the particular choice of MR data algorithms does not affect this work.

As a concluding remark, we wish to underscore the challenging proposition of using MRI to guide such entities inside complex and narrow access paths. Motivated by the inherent low sensitivity of MRI modality that prevents collecting high SNR, and often high CNR, images in real-time, we describe a computational approach that uses MR-based virtual fixtures to set an access corridor that offers an operator assigned safety margin (for a more or less conservative approach) for visual servoing, image-based MRbot control, or force-feedback-assisted manual control. The next step is to develop special MR pulse sequences that will allow faster tracking of the MRbot, as well as refreshment of the path forward its motion. Only with improved real-time sensing may we claim that this robotic technology can contribute to interventional medicine.

# Bibliography

- [1] B. A. T., F. O., H. L., and D. P. E. MRI-powered robotics. In *International Symposium on Robotics Research*, Sestri Levante, Italy, September 2015.
- [2] A. P. Advincula and A. Song. The role of robotic surgery in gynecology. *Current Opinion in Obstetrics and Gynecology*, 19(4):331–336, 2007.
- [3] I. Ahmed, Q. N. U. Rehman, G. Masood, M. Nawaz, A. Adnan, and M. Khan. Segmentation of brain tumor from healthy tissues using multimodal MRI images. *International Journal of Computer Science and Information Security*, 14(10):676, 2016.
- [4] M. Allaf, A. Patriciu, D. Mazilu, L. Kavoussi, and D. Stoianovici. Overview and fundamentals of urologic robot-integrated systems. *Urologic Clinics of North America*, 31(4):671–682, 2004.
- [5] C. A. Anderson, E. Rodriguez, and W. R. Chitwood Jr. Robotically assisted coronary surgery: what is the future? *Current Opinion in Cardiology*, 22(6):541–544, 2007.
- [6] G. H. Ballantyne. Robotic surgery, telerobotic surgery, telepresence, and tele-mentoring. *Surgical Endoscopy*, 16(10):1389–1402, 2002.
- [7] S. Bauer, L.-P. Nolte, and M. Reyes. Fully automatic segmentation of brain tumor images using support vector machine classification in combination with hierarchical conditional random field regularization. In *International Conference on Medical Image Computing and Computer-Assisted Intervention*, pages 354–361. Springer, 2011.
- [8] S. Bauer, R. Wiest, L.-P. Nolte, and M. Reyes. A survey of MRI-based medical image analysis for brain tumor studies. *Physics in Medicine and Biology*, 58(13):R97, 2013.

- [9] A. Becker, G. Habibi, J. Werfel, M. Rubenstein, and J. McLurkin. Massive uniform manipulation: Controlling large populations of simple robots with a common input signal. In *Intelligent Robots and Systems (IROS), 2013 IEEE/RSJ International Conference on*, pages 520–527. IEEE, 2013.
- [10] A. T. Becker, O. Felfoul, and P. E. Dupont. Toward tissue penetration by MRI-powered millirobots using a self-assembled gauss gun. In *Robotics and Automation (ICRA), 2015 IEEE International Conference on*, pages 1184–1189. IEEE, 2015.
- [11] B. T. Bethea, A. M. Okamura, M. Kitagawa, T. P. Fitton, S. M. Cattaneo, V. L. Gott, W. A. Baumgartner, and D. D. Yuh. Application of haptic feedback to robotic surgery. *Journal of Laparoendoscopic & Advanced Surgical Techniques*, 14(3):191–195, 2004.
- [12] M. S. Brown, M. F. McNitt-Gray, J. G. Goldin, R. D. Suh, J. W. Sayre, and D. R. Aberle. Patient-specific models for lung nodule detection and surveillance in CT images. *IEEE Transactions on Medical Imaging*, 20(12):1242–1250, 2001.
- [13] J. W. Cannon, R. D. Howe, P. E. Dupont, J. K. Triedman, G. R. Marx, and J. Pedro. Application of robotics in congenital cardiac surgery. In *Seminars in Thoracic and Cardiovascular Surgery: Pediatric Cardiac Surgery Annual*, volume 6, pages 72–83. Elsevier, 2003.
- [14] R. W. Carlsen, M. R. Edwards, J. Zhuang, C. Pacoret, and M. Sitti. Magnetic steering control of multi-cellular bio-hybrid microswimmers. *Lab on a Chip*, 14(19):3850–3859, 2014.
- [15] P. Casale. Robotic pediatric urology. *Expert review of medical devices*, 5(1):59–64, 2008.
- [16] F. Cepolina, B. Challacombe, and R. C. Michelini. Trends in robotic surgery. *Journal of Endourology*, 19(8):940–951, 2005.
- [17] A. Chanu, O. Felfoul, G. Beaudoin, and S. Martel. Adapting the clinical MRI software environment for real-time navigation of an endovascular untethered ferromagnetic bead for future endovascular interventions. *Magnetic Resonance in medicine*, 59(6):1287–1297, 2008.
- [18] W. R. Chitwood, A. P. Kypson, and L. Nifong. Robotic mitral valve surgery: a technologic and economic revolution for heart centers. *American Heart Hospital Journal*, 1(1):30–39, 2003.

- [19] J. R. Clark, L. Leon, F. M. Warren, and J. J. Abbott. Magnetic guidance of cochlear implants: proof-of-concept and initial feasibility study. *Journal of Medical Devices*, 6(3):035002, 2012.
- [20] A. C. Colchester, J. Zhao, K. S. Holton-Tainter, C. J. Henri, N. Maitland, P. T. Roberts, C. G. Harris, and R. J. Evans. Development and preliminary evaluation of VISLAN, a surgical planning and guidance system using intra-operative video imaging. *Medical Image Analysis*, 1(1):73–90, 1996.
- [21] E. Diller and M. Sitti. Three-dimensional programmable assembly by untethered magnetic robotic micro-grippers. *Advanced Functional Materials*, 24(28):4397–4404, 2014.
- [22] K. Doi. Computer-aided diagnosis in medical imaging: historical review, current status and future potential. *Computerized Medical Imaging and Graphics*, 31(4):198–211, 2007.
- [23] K. Doi. Current status and future potential of computer-aided diagnosis in medical imaging. *The British Journal of Radiology*, 2014.
- [24] E. C. Fear, X. Li, S. C. Hagness, and M. A. Stuchly. Confocal microwave imaging for breast cancer detection: Localization of tumors in three dimensions. *IEEE Transactions on Biomedical Engineering*, 49(8):812–822, 2002.
- [25] O. Felfoul, A. Becker, C. Bergeles, and P. E. Dupont. Achieving commutation control of an MRI-powered robot actuator. *IEEE Transactions on Robotics*, 31(2):387–399, 2015.
- [26] O. Felfoul, A. T. Becker, G. Fagogenis, and P. E. Dupont. Simultaneous steering and imaging of magnetic particles using MRI toward delivery of therapeutics. *Scientific Reports*, 6, 2016.
- [27] O. Felfoul, J.-B. Mathieu, G. Beaudoin, and S. Martel. In vivo MR-tracking based on magnetic signature selective excitation. *IEEE Transactions on Medical Imaging*, 27(1):28–35, 2008.
- [28] F. Filsoufi, L. Aklog, and D. H. Adams. Minimally invasive CABG. *Current Opinion in Cardiology*, 16(5):306–309, 2001.
- [29] G. S. Fischer, A. Krieger, I. Iordachita, C. Csoma, L. L. Whitcomb, and G. Fichtinger. MRI compatibility of robot actuation techniques—a comparative study. In *International Conference on Medical Image Computing and Computer-Assisted Intervention*, pages 509–517. Springer, 2008.

- [30] I. J. Fox, G. Q. Daley, S. A. Goldman, J. Huard, T. J. Kamp, and M. Trucco. Use of differentiated pluripotent stem cells in replacement therapy for treating disease. *Science*, 345(6199):1247391, 2014.
- [31] A. F. Frangi, W. J. Niessen, K. L. Vincken, and M. A. Viergever. Multi-scale vessel enhancement filtering. In *International Conference on Medical Image Computing and Computer-Assisted Intervention*, pages 130–137. Springer, 1998.
- [32] K. Fuchs. Minimally invasive surgery. *Endoscopy*, 34(02):154–159, 2002.
- [33] S. Fusco, G. Chatzipirpiridis, K. M. Sivaraman, O. Ergeneman, B. J. Nelson, and S. Pané. Chitosan electrodeposition for microrobotic drug delivery. *Advanced Healthcare Materials*, 2(7):1037–1044, 2013.
- [34] J. Giltinan, E. Diller, C. Mayda, and M. Sitti. Three-dimensional robotic manipulation and transport of micro-scale objects by a magnetically driven capillary micro-gripper. In *Robotics and Automation (ICRA), 2014 IEEE International Conference on*, pages 2077–2082. IEEE, 2014.
- [35] N. Gordillo, E. Montseny, and P. Sobrevilla. State of the art survey on MRI brain tumor segmentation. *Magnetic Resonance Imaging*, 31(8):1426–1438, 2013.
- [36] H. Gudbjartsson and S. Patz. The rician distribution of noisy MRI data. *Magnetic Resonance in Medicine*, 34(6):910–914, 1995.
- [37] L. O. Hall, A. M. Bensaid, L. P. Clarke, R. P. Velthuizen, M. S. Silbiger, and J. C. Bezdek. A comparison of neural network and fuzzy clustering techniques in segmenting magnetic resonance images of the brain. *IEEE Transactions on Neural Networks*, 3(5):672–682, 1992.
- [38] E. J. Hanly and M. A. Talamini. Robotic abdominal surgery. *The American Journal of Surgery*, 188(4):19–26, 2004.
- [39] M. Hashizume, K. Konishi, N. Tsutsumi, S. Yamaguchi, and R. Shimabukuro. A new era of robotic surgery assisted by a computer-enhanced surgical system. *Surgery*, 131(1):S330–S333, 2002.
- [40] A. T. Hillel, A. Kapoor, N. Simaan, R. H. Taylor, and P. Flint. Applications of robotics for laryngeal surgery. *Otolaryngologic Clinics of North America*, 41(4):781–791, 2008.

- [41] M. Ho, A. B. McMillan, J. M. Simard, R. Gullapalli, and J. P. Desai. Toward a meso-scale SMA-actuated MRI-compatible neurosurgical robot. *IEEE Transactions on Robotics*, 28(1):213–222, 2012.
- [42] S. Ho, E. Bullitt, and G. Gerig. Level-set evolution with region competition: automatic 3D segmentation of brain tumors. In *Pattern Recognition, 2002. Proceedings. 16th International Conference on*, volume 1, pages 532–535. IEEE, 2002.
- [43] A. Hoover, V. Kouznetsova, and M. Goldbaum. Locating blood vessels in retinal images by piecewise threshold probing of a matched filter response. *IEEE Transactions on Medical imaging*, 19(3):203–210, 2000.
- [44] R. D. Howe and Y. Matsuoka. Robotics for surgery. *Annual Review of Biomedical Engineering*, 1(1):211–240, 1999.
- [45] A. Hoznek, R. Katz, M. Gettman, L. Salomon, P. Antiphon, A. de la Taille, R. Yiou, D. Chopin, and C.-C. Abbou. Laparoscopic and robotic surgical training in urology. *Current Urology Reports*, 4(2):130–137, 2003.
- [46] K. M. Iftexharuddin, J. Zheng, M. A. Islam, and R. J. Ogg. Fractal-based brain tumor detection in multimodal MRI. *Applied Mathematics and Computation*, 207(1):23–41, 2009.
- [47] G. Jacobsen, F. Elli, and S. Horgan. Robotic surgery update. *Surgical Endoscopy And Other Interventional Techniques*, 18(8):1186–1191, 2004.
- [48] M. T. Karamessini, G. C. Kagadis, T. Petsas, D. Karnabatidis, D. Konstantinou, G. C. Sakellaropoulos, G. C. Nikiforidis, and D. Siablis. CT angiography with three-dimensional techniques for the early diagnosis of intracranial aneurysms. comparison with intra-arterial DSA and the surgical findings. *European Journal of Radiology*, 49(3):212–223, 2004.
- [49] H. Khotanlou, O. Colliot, J. Atif, and I. Bloch. 3d brain tumor segmentation in MRI using fuzzy classification, symmetry analysis and spatially constrained deformable models. *Fuzzy Sets and Systems*, 160(10):1457–1473, 2009.
- [50] R. Kikinis, C. R. Guttmann, D. Metcalf, W. M. Wells, G. J. Ettinger, H. L. Weiner, and F. A. Jolesz. Quantitative follow-up of patients with multiple sclerosis using MRI: technical aspects. *Journal of Magnetic Resonance Imaging*, 9(4):519–530, 1999.

- [51] C. Kirbas and F. Quek. A review of vessel extraction techniques and algorithms. *ACM Computing Surveys (CSUR)*, 36(2):81–121, 2004.
- [52] M. F. Kircher, A. De La Zerda, J. V. Jokerst, C. L. Zavaleta, P. J. Kempen, E. Mittra, K. Pitter, R. Huang, C. Campos, F. Habte, et al. A brain tumor molecular imaging strategy using a new triple-modality MRI-photoacoustic-raman nanoparticle. *Nature Medicine*, 18(5):829–834, 2012.
- [53] G. Kósa, P. Jakab, G. Székely, and N. Hata. MRI driven magnetic microswimmers. *Biomedical microdevices*, 14(1):165–178, 2012.
- [54] A. P. Kypson, L. W. Nifong, and W. R. Chitwood. Robotic mitral valve surgery. In *Seminars in Thoracic and Cardiovascular Surgery*, volume 15, pages 121–129. Elsevier, 2003.
- [55] A. P. Kypson, L. W. Nifong, and W. R. Chitwood Jr. Robotic cardiac surgery. *Journal of Long-term Effects of Medical Implants*, 13(6), 2003.
- [56] D. Lesage, E. D. Angelini, I. Bloch, and G. Funka-Lea. A review of 3D vessel lumen segmentation techniques: Models, features and extraction schemes. *Medical Image Analysis*, 13(6):819–845, 2009.
- [57] T. Liu and M. C. Çavuşoğlu. Three dimensional modeling of an MRI actuated steerable catheter system. In *Robotics and Automation (ICRA), 2014 IEEE International Conference on*, pages 4393–4398. IEEE, 2014.
- [58] L. Lukas, A. Devos, J. A. Suykens, L. Vanhamme, F. A. Howe, C. Majós, A. Moreno-Torres, M. Van der Graaf, A. R. Tate, C. Arús, et al. Brain tumor classification based on long echo proton MRS signals. *Artificial Intelligence in Medicine*, 31(1):73–89, 2004.
- [59] I. Macía, M. Graña, J. Maiora, C. Paloc, and M. De Blas. Detection of type ii endoleaks in abdominal aortic aneurysms after endovascular repair. *Computers in Biology and Medicine*, 41(10):871–880, 2011.
- [60] I. Macía, J. H. Legarreta, C. Paloc, M. Graña, J. Maiora, G. García, and M. De Blas. Segmentation of abdominal aortic aneurysms in CT images using a radial model approach. In *International Conference on Intelligent Data Engineering and Automated Learning*, pages 664–671. Springer, 2009.
- [61] R. J. Maciunas. Computer-assisted neurosurgery. *Clinical Neurosurgery*, 53:267, 2006.

- [62] F. Maes, D. Vandermeulen, and P. Suetens. Medical image registration using mutual information. *Proceedings of the IEEE*, 91(10):1699–1722, 2003.
- [63] J. F. Magrina. Robotic surgery in gynecology. *European Journal of Gynaecological Oncology*, 28(2):77–82, 2006.
- [64] J. A. Maintz and M. A. Viergever. A survey of medical image registration. *Medical Image Analysis*, 2(1):1–36, 1998.
- [65] S. Martel. Bacterial microsystems and microrobots. *Biomedical Microdevices*, 14(6):1033–1045, 2012.
- [66] S. Martel. Microrobotics in the vascular network: present status and next challenges. *Journal of Micro-Bio Robotics*, 8(1):41–52, 2013.
- [67] S. Martel, J.-B. Mathieu, O. Felfoul, A. Chanu, E. Aboussouan, S. Tamaz, P. Pouponneau, L. Yahia, G. Beaudoin, G. Soulez, et al. Automatic navigation of an untethered device in the artery of a living animal using a conventional clinical magnetic resonance imaging system. *Applied Physics Letters*, 90(11):114105, 2007.
- [68] B. D. Martinez and C. S. Wiegand. Robotics in vascular surgery. *The American Journal of Surgery*, 188(4):57–62, 2004.
- [69] J.-B. Mathieu, G. Beaudoin, and S. Martel. Method of propulsion of a ferromagnetic core in the cardiovascular system through magnetic gradients generated by an MRI system. *IEEE Transactions on Biomedical Engineering*, 53(2):292–299, 2006.
- [70] P. Miloro, E. Sinibaldi, A. Menciasci, and P. Dario. Removing vascular obstructions: a challenge, yet an opportunity for interventional microdevices. *Biomedical Microdevices*, 14(3):511–532, 2012.
- [71] F. Munoz, G. Alici, and W. Li. A review of drug delivery systems for capsule endoscopy. *Advanced Drug Delivery Reviews*, 71:77–85, 2014.
- [72] P. Mussio, M. Pietrogrande, P. Bottoni, M. Dell’Oca, E. Arosio, E. Sartirana, M. Finanzon, and N. Dioguardi. Automatic cell count in digital images of liver tissue sections. In *Computer-Based Medical Systems, 1991. Proceedings of the Fourth Annual IEEE Symposium*, pages 153–160. IEEE, 1991.
- [73] A. Mustaqeem, A. Javed, and T. Fatima. An efficient brain tumor detection algorithm using watershed & thresholding based segmentation. *International Journal of Image, Graphics and Signal Processing*, 4(10):34, 2012.

- [74] N. V. Navkar, N. V. Tsekos, J. R. Stafford, J. S. Weinberg, and Z. Deng. Visualization and planning of neurosurgical interventions with straight access. In *International Conference on Information Processing in Computer-Assisted Interventions*, pages 1–11. Springer, 2010.
- [75] D. Oleynikov. Robotic surgery. *Surgical Clinics of North America*, 88(5):1121–1130, 2008.
- [76] A. Padma and R. Sukanesh. Automatic classification and segmentation of brain tumor in CT images using optimal dominant gray level run length texture features. *International Journal of Advanced Computer Science and Applications*, 2(10), 2011.
- [77] R. Patel and P. Casale. Robotic pediatric urology. *Minerva Urologica e Nefrologica= The Italian Journal of Urology and Nephrology*, 59(4):425–430, 2007.
- [78] S. Pereira, A. Oliveira, V. Alves, and C. A. Silva. On hierarchical brain tumor segmentation in MRI using fully convolutional neural networks: A preliminary study. In *Bioengineering (ENBENG), 2017 IEEE 5th Portuguese Meeting on*, pages 1–4. IEEE, 2017.
- [79] D. L. Pham, C. Xu, and J. L. Prince. Current methods in medical image segmentation 1. *Annual Review of Biomedical Engineering*, 2(1):315–337, 2000.
- [80] R. Pohle and K. D. Toennies. Segmentation of medical images using adaptive region growing. In *Medical Imaging 2001*, pages 1337–1346. International Society for Optics and Photonics, 2001.
- [81] M. Prastawa, E. Bullitt, S. Ho, and G. Gerig. A brain tumor segmentation framework based on outlier detection. *Medical Image Analysis*, 8(3):275–283, 2004.
- [82] S. Preethi. VLSI implementation of brain tumor segmentation using fuzzy C-mean clustering. *Networking and Communication Engineering*, 9(3):56–58, 2017.
- [83] R. Ratan, S. Sharma, and S. Sharma. Brain tumor detection based on multi-parameter MRI image analysis. *ICGST-GVIP Journal*, 9(3):9–17, 2009.
- [84] H. Refai, L. Li, T. K. Teague, and R. Naukam. Automatic count of hepatocytes in microscopic images. In *Image Processing, 2003. ICIP 2003. Proceedings. 2003 International Conference on*, volume 2, pages II–1101. IEEE, 2003.

- [85] J. Rogowska. Overview and fundamentals of medical image segmentation-5. In I. Bankman, editor, *Handbook of Medical Imaging: Processing and Analysis Management*, pages 69–85. Academic Press, 2000.
- [86] S. Ruan, S. Lebonvallet, A. Merabet, and J.-M. Constans. Tumor segmentation from a multispectral MRI images by using support vector machine classification. In *Biomedical Imaging: From Nano to Macro, 2007. ISBI 2007. 4th IEEE International Symposium on*, pages 1236–1239. IEEE, 2007.
- [87] J. C. Russ and F. B. Neal. *The image processing handbook*. CRC Press, Inc. Boca Raton, FL, USA, 7th edition, 2015.
- [88] J. Sachdeva, V. Kumar, I. Gupta, N. Khandelwal, and C. K. Ahuja. A novel content-based active contour model for brain tumor segmentation. *Magnetic Resonance Imaging*, 30(5):694–715, 2012.
- [89] M. G. Schouten, J. G. Bomers, D. Yakar, H. Huisman, E. Rothgang, D. Bosboom, T. W. Scheenen, S. Misra, and J. J. Fütterer. Evaluation of a robotic technique for transrectal mri-guided prostate biopsies. *European Radiology*, 22(2):476–483, 2012.
- [90] M. Schurr, G. Buess, B. Neisius, and U. Voges. Robotics and telemanipulation technologies for endoscopic surgery. *Surgical Endoscopy*, 14(4):375–381, 2000.
- [91] J. Selvakumar, A. Lakshmi, and T. Arivoli. Brain tumor segmentation and its area calculation in brain MR images using K-mean clustering and fuzzy C-mean algorithm. In *Advances in Engineering, Science and Management (ICAESM), 2012 International Conference on*, pages 186–190. IEEE, 2012.
- [92] N. Sharma, L. M. Aggarwal, et al. Automated medical image segmentation techniques. *Journal of Medical Physics*, 35(1):3, 2010.
- [93] W. Shitong and W. Min. A new detection algorithm (NDA) based on fuzzy cellular neural networks for white blood cell detection. *IEEE Transactions on Information Technology in Biomedicine*, 10(1):5–10, 2006.
- [94] H. G. Sim, S. K. H. Yip, and C. W. S. Cheng. Equipment and technology in surgical robotics. *World Journal of Urology*, 24(2):128–135, 2006.
- [95] A. W. Simonetti, W. J. Melssen, F. S. d. Edelenyi, J. J. van Asten, A. Heerschap, and L. Buydens. Combination of feature-reduced MR spectroscopic and MR imaging data for improved brain tumor classification. *NMR in Biomedicine*, 18(1):34–43, 2005.

- [96] A. W. Simonetti, W. J. Melssen, M. van der Graaf, G. J. Postma, A. Heerschap, and L. M. Buydens. A chemometric approach for brain tumor classification using magnetic resonance imaging and spectroscopy. *Analytical Chemistry*, 75(20):5352–5361, 2003.
- [97] M. Sitti, H. Ceylan, W. Hu, J. Giltinan, M. Turan, S. Yim, and E. Diller. Biomedical applications of untethered mobile milli/microrobots. *Proceedings of the IEEE*, 103(2):205–224, 2015.
- [98] J. V. Soares, J. J. Leandro, R. M. Cesar, H. F. Jelinek, and M. J. Cree. Retinal vessel segmentation using the 2D gabor wavelet and supervised classification. *IEEE Transactions on Medical Imaging*, 25(9):1214–1222, 2006.
- [99] D. Y. Song, E. C. Burdette, J. Fiene, E. Armour, G. Kronreif, A. Deguet, Z. Zhang, I. Iordachita, G. Fichtinger, and P. Kazanzides. Robotic needle guide for prostate brachytherapy: clinical testing of feasibility and performance. *Brachytherapy*, 10(1):57–63, 2011.
- [100] T. Spencer, J. A. Olson, K. C. McHardy, P. F. Sharp, and J. V. Forrester. An image-processing strategy for the segmentation and quantification of microaneurysms in fluorescein angiograms of the ocular fundus. *Computers and Biomedical Research*, 29(4):284–302, 1996.
- [101] R. N. Strickland. *Image-processing techniques for tumor detection*. CRC Press, 2002.
- [102] H. Su, D. C. Cardona, W. Shang, A. Camilo, G. A. Cole, D. C. Rucker, R. J. Webster, and G. S. Fischer. A MRI-guided concentric tube continuum robot with piezoelectric actuation: a feasibility study. In *Robotics and Automation (ICRA), 2012 IEEE International Conference on*, pages 1939–1945. IEEE, 2012.
- [103] J. S. Suri, K. Liu, L. Reden, and S. Laxminarayan. A review on MR vascular image processing algorithms: acquisition and prefiltering: part I. *IEEE Transactions on Information Technology in Biomedicine: a publication of the IEEE Engineering in Medicine and Biology Society*, 6(4):324–337, 2002.
- [104] S. Tasoglu, E. Diller, S. Guven, M. Sitti, and U. Demirci. Untethered micro-robotic coding of three-dimensional material composition. *Nature Communications*, 5, 2014.

- [105] M. Tavakoli, R. Patel, and M. Moallem. Haptic interaction in robot-assisted endoscopic surgery: a sensorized end-effector. *The International Journal of Medical Robotics and Computer Assisted Surgery*, 1(2):53–63, 2005.
- [106] D. Teber, M. Baumhauer, E. O. Guven, and J. Rassweiler. Robotic and imaging in urological surgery. *Current Opinion in Urology*, 19(1):108–113, 2009.
- [107] S. Tognarelli, V. Castelli, G. Ciuti, C. Di Natali, E. Sinibaldi, P. Dario, and A. Menciassi. Magnetic propulsion and ultrasound tracking of endovascular devices. *Journal of Robotic Surgery*, 6(1):5–12, 2012.
- [108] F. Ullrich, C. Bergeles, J. Pokki, O. Ergeneman, S. Erni, G. Chatzipirpiridis, S. Pané, C. Framme, and B. J. Nelson. Mobility experiments with microrobots for minimally invasive intraocular surgery. *Investigative Ophthalmology & Visual Science*, 54(4):2853–2863, 2013.
- [109] P. A. Van den Elsen, E.-J. Pol, and M. A. Viergever. Medical image matching—a review with classification. *IEEE Engineering in Medicine and Biology Magazine*, 12(1):26–39, 1993.
- [110] O. Van der Meijden and M. Schijven. The value of haptic feedback in conventional and robot-assisted minimal invasive surgery and virtual reality training: a current review. *Surgical Endoscopy*, 23(6):1180–1190, 2009.
- [111] I. M. Varkarakis, S. Rais-Bahrami, L. R. Kavoussi, and D. Stoianovici. Robotic surgery and telesurgery in urology. *Urology*, 65(5):840–846, 2005.
- [112] P. Vartholomeos, C. Bergeles, L. Qin, and P. E. Dupont. An MRI-powered and controlled actuator technology for tetherless robotic interventions. *The International Journal of Robotics Research*, 32(13):1536–1552, 2013.
- [113] P. Vartholomeos, L. Qin, and P. E. Dupont. MRI-powered actuators for robotic interventions. In *Intelligent Robots and Systems (IROS), 2011 IEEE/RSJ International Conference on*, pages 4508–4515. IEEE, 2011.
- [114] A. G. Visco and A. P. Advincula. Robotic gynecologic surgery. *Obstetrics & Gynecology*, 112(6):1369–1384, 2008.
- [115] T. Walter, J.-C. Klein, P. Massin, and A. Erginay. A contribution of image processing to the diagnosis of diabetic retinopathy—detection of exudates in color fundus images of the human retina. *IEEE Transactions on Medical Imaging*, 21(10):1236–1243, 2002.

- [116] K. Xie, J. Yang, Z. Zhang, and Y. Zhu. Semi-automated brain tumor and edema segmentation using MRI. *European Journal of Radiology*, 56(1):12–19, 2005.
- [117] S. Yim, E. Gultepe, D. H. Gracias, and M. Sitti. Biopsy using a magnetic capsule endoscope carrying, releasing, and retrieving untethered microgrippers. *IEEE Transactions on Biomedical Engineering*, 61(2):513–521, 2014.
- [118] S. Yim and M. Sitti. Design and rolling locomotion of a magnetically actuated soft capsule endoscope. *IEEE Transactions on Robotics*, 28(1):183–194, 2012.
- [119] C. Yu, J. Kim, H. Choi, J. Choi, S. Jeong, K. Cha, J.-o. Park, and S. Park. Novel electromagnetic actuation system for three-dimensional locomotion and drilling of intravascular microrobot. *Sensors and Actuators A: Physical*, 161(1):297–304, 2010.